PHYSICAL REVIEW D **88,** 094508 (2013)

Finite size scaling study of $N_f = 4$ finite density QCD on the lattice

Xiao-Yong Jin (金曉勇),[1] Yoshinobu Kuramashi (藏増嘉伸),[2,3,1] Yoshifumi Nakamura (中村宜文),[1] Shinji Takeda (武田真滋),[4,1] and Akira Ukawa (宇川彰)[3,1]

[1]*RIKEN Advanced Institute for Computational Science, Kobe, Hyogo 650-0047, Japan*
[2]*Faculty of Pure and Applied Sciences, University of Tsukuba, Tsukuba, Ibaraki 305-8571, Japan*
[3]*Center for Computational Sciences, University of Tsukuba, Tsukuba, Ibaraki 305-8577, Japan*
[4]*Institute of Physics, Kanazawa University, Kanazawa 920-1192, Japan*
(Received 30 July 2013; published 22 November 2013)

We explore the phase space spanned by the temperature and the chemical potential for four-flavor lattice QCD using the Wilson-clover quark action. In order to determine the order of the phase transition, we apply finite-size scaling analyses to gluonic and quark observables, including plaquette, Polyakov loop, and quark number density, and examine their susceptibility, skewness, kurtosis, and Challa-Landau-Binder cumulant. Simulations were carried out on lattices of a temporal size fixed at $N_t = 4$ and spatial sizes chosen from 6^3 up to 10^3. Configurations were generated using the phase-reweighting approach, while the value of the phase of the quark determinant was carefully monitored. The μ-parameter reweighting technique is employed to precisely locate the point of the phase transition. Among various approximation schemes for calculating the ratio of quark determinants needed for μ reweighting, we found the Taylor expansion of the logarithm of the quark determinant to be the most reliable. Our finite-size analyses show that the transition is first order at $(\beta, \kappa, \mu/T) = (1.58, 0.1385, 0.584 \pm 0.008)$, where $(m_\pi/m_\rho, T/m_\rho) = (0.822, 0.154)$. It weakens considerably at $(\beta, \kappa, \mu/T) = (1.60, 0.1371, 0.821 \pm 0.008)$, where $(m_\pi/m_\rho, T/m_\rho) = (0.839, 0.150)$, and a crossover rather than a first-order phase transition cannot be ruled out.

DOI: 10.1103/PhysRevD.88.094508 PACS numbers: 12.38.Gc

I. INTRODUCTION

The four-flavor QCD is a good testing ground for finite temperature and chemical potential analyses before studying the physically more relevant case of the three-flavor theory. In fact, since the four-flavor theory can be described with the staggered fermion formalism without rooting, new ideas to explore QCD with finite density have first been tried out in this theory [1–3].

More fundamentally, the phase diagram of the four-flavor theory is expected to have a structure well suited for exploratory studies at finite density. With massless quarks, as shown in Fig. 1(a), a continuous line of first-order phase transitions connects the temperature and chemical potential axes. When the quark mass, m_q, is increased, the first-order phase transition at zero density turns into a crossover beyond some value of m_q [4–8], while the transition at zero temperature and finite density remains first order as shown in Fig. 1(b). Consequently the first-order line up to some value of the chemical potential also turns into a crossover. Hence a critical end point is expected at a finite chemical potential, which is reminiscent of the situation for the three-flavor theory with the physical spectrum of up, down, and strange quarks. It is empirically known [9,10] in the zero-density case that the first-order phase transition persists up to a relatively large quark mass in the four-flavor theory. Therefore, one should be able to probe the region of the transition line with a reasonable computational cost and learn much about the physical characteristics of the transition before tackling a more difficult three-flavor theory.

A powerful method for resolving the nature of phase transition is the finite-size scaling analysis. While this method has been extensively exploited in lattice QCD studies at finite temperatures, the situation appears quite different at nonzero baryon density. This is partly due to the fact that in the phase-reweighting procedure for numerical simulations at nonzero density, the averaged phase-reweighting factor is expected to decrease exponentially as the lattice volume increases, leading to a loss of control of statistical averages of observables. In addition, the calculation of the quark determinant necessary for evaluating the phase is computationally very expensive.

We note, however, that the former problem does not necessarily preclude finite-size scaling analyses as long as the reweighting factor stays reasonably away from zero over the range of lattice volumes needed for the analysis. This is a dynamical question, and as we have shown in Ref. [11], the averaged phase-reweighting factor becomes larger for larger temporal lattice sizes. Concerning the latter, the reduction of the quark determinant [12–14] and the recent development of computing technology including high-speed general-purpose computing on graphics processing units have significantly extended the range of lattice sizes for which the determinant is calculable in practice. In this paper we therefore make a serious attempt at finite- size scaling analyses for nonzero-density QCD.

The Kentucky group [15] studied the phase structure of the four-flavor theory using the canonical approach employing the Wilson-clover quark action. They observed an S-shaped structure in the chemical potential versus quark

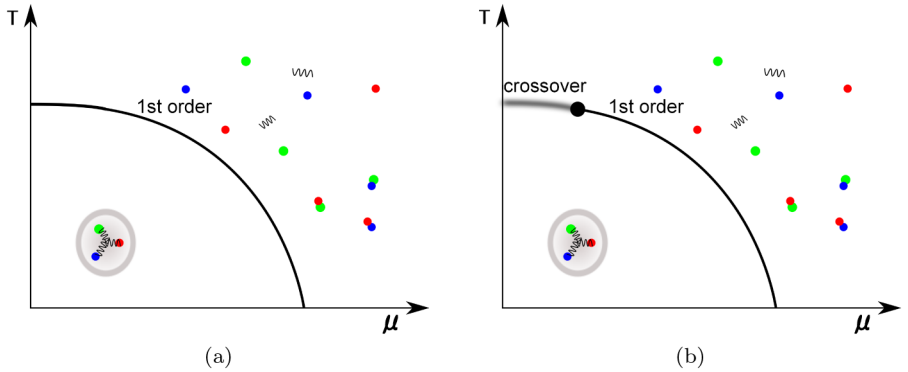

FIG. 1 (color online). Phase diagram on the (μ, T) plane expected for four-flavor QCD for (a) massless quarks and (b) heavy quarks.

number plot, which they took to be an indication of a first-order phase transition. The study was only on a single lattice volume of $6^3 \times 4$ and with relatively low statistics, however, so this may not be taken as a conclusive statement. From the point of view of universality, it is important to check the phase structure by using different approaches. Accordingly, we also employed the Wilson-clover quark action, but adopted the grand canonical approach and performed a finite-size scaling study to learn how we can quantitatively resolve the order of the transition.

The rest of the paper is organized as follows. We briefly discuss the phase-reweighting method and parameter reweighting for μ in Secs. II and III, respectively. Simulation parameters are summarized in Sec. IV. After defining the observables we measure in Sec. V, we present our finite-size scaling analysis using susceptibility, skewness, kurtosis, and the Challa-Landau-Binder cumulant for a variety of gluonic and quark observables in Sec. VI. By combining with results of zero-density simulation, we describe a sketch of the global phase diagram in Sec. VII. In the last section, we present our concluding remarks. In Appendix A we summarize an analysis of volume scaling of higher moments by using a double Gaussian distribution model, and in Appendix B some details of μ reweighting for observables that explicitly depend on μ are given.

Throughout this paper we consider a four-dimensional Euclidean lattice of a size specified by $N_x \times N_y \times N_z \times N_t$. The boundary condition is periodic in the spatial directions, while in the temporal direction, it is periodic (antiperiodic) for gluon (quark) fields. Some preliminary results given in this paper were already reported at the Lattice 2012 Conference [16].

II. PHASE REWEIGHTING

Physics of QCD for finite quark chemical potential μ can be studied by the grand canonical partition function. Assuming that the N_f quark flavors are degenerate, i.e., all quarks have the same mass and chemical potential, the partition function is given by

$$Z_{\mathrm{QCD}}(\mu) = \int [dU] e^{-S_G} \det D(\mu)^{N_f}, \tag{1}$$

$$= \int [dU] \exp(-S_{\mathrm{QCD}}), \tag{2}$$

$$S_{\mathrm{QCD}} = S_G - N_f \ln \det D(\mu). \tag{3}$$

We adopt the Wilson-clover quark action with the Wilson-Dirac matrix,

$$\begin{aligned} D(\mu) = \delta_{x,y} - \kappa \sum_{\nu=1}^{4} [& e^{\mu a \delta_{\nu,4}} (1 - \gamma_\nu) U(x, \nu) \delta_{x+\hat{\nu},y} \\ & + e^{-\mu a \delta_{\nu,4}} (1 + \gamma_\nu) U(y, \nu)^\dagger \delta_{x-\hat{\nu},y}] \\ & + \kappa c_{\mathrm{sw}} \delta_{x,y} F_{\nu\rho}(x) \sigma_{\nu\rho}, \end{aligned} \tag{4}$$

with μ the chemical potential, a the lattice spacing, and $F_{\nu\rho}(x)$ the standard clover term. We employ the Iwasaki gauge action [17]

$$\begin{aligned} S_G = \beta \sum_x \Big\{ & c_0 \sum_{\nu<\rho} \left(1 - \frac{1}{3} \mathrm{Re} W^{1\times1}_{\nu\rho}(x)\right) \\ & + c_1 \sum_{\nu,\rho} \left(1 - \frac{1}{3} \mathrm{Re} W^{1\times2}_{\nu\rho}(x)\right) \Big\}, \end{aligned} \tag{5}$$

with $c_1 = -0.331$, $c_0 = 1 - 8c_1 = 3.648$, and the gauge invariant loops are given by

$$W^{1\times1}_{\nu\rho}(x) = \mathrm{tr}[U(x, \nu) U(x + \hat{\nu}, \rho) U(x + \hat{\rho}, \nu)^\dagger U(x, \rho)^\dagger], \tag{6}$$

$$\begin{aligned} W^{1\times2}_{\nu\rho}(x) = \mathrm{tr}[& U(x, \nu) U(x + \hat{\nu}, \rho) U(x + \hat{\nu} \\ & + \hat{\rho}, \rho) U(x + 2\hat{\rho}, \nu)^\dagger U(x + \hat{\rho}, \rho)^\dagger U(x, \rho)^\dagger]. \end{aligned} \tag{7}$$

Since the quark determinant with $\mu \neq 0$ is complex, one cannot apply the standard Monte Carlo simulation. Defining the phase of the quark determinant with

$$\det D(\mu) \equiv |\det D(\mu)| e^{i\theta(\mu)}, \tag{8}$$

one can rewrite the expectation value of an observable $\mathcal{O}$ as

$$\langle \mathcal{O} \rangle = \frac{\langle \mathcal{O} e^{iN_f\theta} \rangle_{||}}{\langle e^{iN_f\theta} \rangle_{||}}, \tag{9}$$

where the phase-included and the phase-quenched ensemble averages are given by

$$\langle \mathcal{O} \rangle = \frac{\int [dU] e^{-S_G} (\det D)^{N_f} \mathcal{O}[U]}{\int [dU] e^{-S_G} (\det D)^{N_f}}, \tag{10}$$

$$\langle \mathcal{O} \rangle_{||} = \frac{\int [dU] e^{-S_G} |\det D|^{N_f} \mathcal{O}[U]}{\int [dU] e^{-S_G} |\det D|^{N_f}}. \tag{11}$$

This defines the phase-reweighting method, which allows evaluation of observables as long as the averaged phase-reweighting factor $\langle e^{iN_f\theta} \rangle_{||}$ stays nonzero. In general, this factor vanishes exponentially with the space-time lattice volume, leading to the sign problem. In practice, however, the numerical magnitude of the averaged phase-reweighting factor is dynamically determined. Hence, viability of the phase-reweighting method can only be determined by actual simulations. Furthermore, we have shown in Ref. [11] that the averaged phase-reweighting factor increases for larger temporal lattice sizes, with other parameters fixed in the heavy quark mass region. Therefore, we expect that the phase-reweighting method provides information on the phase structure over the practically useful parameter region.

Another practical issue of the phase-reweighting method is how to compute the phase factor which requires a computationally expensive calculation of the determinant. In order to avoid introduction of systematic errors, we perform an exact calculation of the quark determinant by adopting the reduction technique of Ref. [12]. After reduction in the temporal direction, the quark determinant can be expressed as

$$\begin{aligned} \det D(\mu) &= A_0 W(\mu/T) \\ &= A_0 \det[1 - H_0 - e^{\mu/T} H_+ - e^{-\mu/T} H_-], \end{aligned} \tag{12}$$

where the definition of A_0, $H_\pm$, and H_0 are given in Ref. [11]. After numerically building $H_\pm$ and H_0, which are dense matrices of order $12 N_x N_y N_z$, the determinant in Eq. (12) can be computed by using the LU decomposition. We also perform a reduction in the spinor space. In total, the number of floating point operations for calculating the determinant is reduced by about a factor of two compared to the nonreduced case. In our simulations we exploit general-purpose computing on graphics processing units to carry out the determinant calculation in the reduced form.

III. μ REWEIGHTING

In finite-size scaling analyses we often need to calculate the position of extrema of moments of observables. Since they are usually not located at the points of simulation, reweighting methods as originally proposed in Ref. [18] are very useful. In our case, we want to evaluate physical quantities at a chemical potential μ' from phase-quenched configurations generated at a value $\mu \neq \mu'$. For this purpose, we can use the identity

$$\langle \mathcal{O}(\mu') \rangle_{\mu'} = \frac{\langle \mathcal{O}(\mu') \frac{\det D(\mu')^{N_f}}{\det D(\mu)^{N_f}} e^{iN_f\theta(\mu)} \rangle_{||\mu}}{\langle \frac{\det D(\mu')^{N_f}}{\det D(\mu)^{N_f}} e^{iN_f\theta(\mu)} \rangle_{||\mu}}, \tag{13}$$

where the phase-quenched average at μ in the right-hand side is defined in Eq. (11).

A practical question here is how to evaluate the ratio of quark determinants. Due to its huge computational cost, we have to avoid a direct computation of the full determinant at each reweighted value of the chemical potential. Instead, we exploit an approximation to the determinant and introduce three expansion schemes: winding expansion, Taylor expansion of the determinant, and Taylor expansion of the logarithm of the determinant. In a study of the canonical approach, the expansion of the logarithm of the determinant in terms of the winding number was tested in Ref. [19]. The Taylor expansion of the logarithm of the determinant was used in Ref. [20] for a study of μ reweighting from zero density.

As shown in Eq. (12), the μ dependence of the determinant is factorized, and A_0 does not appear in the ratio of the determinants,

$$\frac{\det D(\mu')^{N_f}}{\det D(\mu)^{N_f}} = \frac{W(\mu'/T)^{N_f}}{W(\mu/T)^{N_f}}. \tag{14}$$

In the following we consider only $W(\mu/T)$.

The winding expansion [12] is an expansion of $\log W(\mu/T)$ in terms of fugacity $\exp \mu/T$;

$$W(\mu/T) = \exp\left[-V \sum_{q \in \mathbb{Z}} v^{(q)} e^{q\mu/T} \right], \tag{15}$$

where the lattice spatial volume V is factored out in the argument. In an actual implementation, one has to truncate the expansion at some order $q = q_{\mathrm{trunc}}$. The approximated form of the ratio is given by

$$\begin{aligned} \frac{\det D(\mu')^{N_f}}{\det D(\mu)^{N_f}} \to \exp\Bigg[& -N_f V \sum_{q=1}^{q_{\mathrm{trunc}}} 2\mathrm{Re}[v^{(q)}] \{\cosh(q\mu'/T) \\ & - \cosh(q\mu/T)\} - iN_f V \sum_{q=1}^{q_{\mathrm{trunc}}} 2\mathrm{Im}[v^{(q)}] \\ & \times \{\sinh(q\mu'/T) - \sinh(q\mu/T)\} \Bigg]. \end{aligned} \tag{16}$$

The second line is considered as an additional phase difference between two fermion determinants. The $v^{(q)}$'s are constructed from H_0 and $H_\pm$ in Eq. (12). In practice we choose $q_{\mathrm{trunc}} = 10$.

In order to define Taylor expansions, we introduce two types of derivatives, Q_n defined by

$$Q_n = \frac{1}{W^{N_f}} \frac{\partial^n W^{N_f}}{\partial(\mu/T)^n} \tag{17}$$

and W_n by

$$\frac{\partial^n \ln W^{N_f}}{\partial(\mu/T)^n} = N_f W_n. \tag{18}$$

These two derivatives can be related to each other as moments and their cumulants. Up to $n = 1, 2, 3, 4$, the relations take the form

$$Q_1 = N_f W_1, \tag{19a}$$
$$Q_2 = N_f W_2 + (N_f W_1)^2, \tag{19b}$$
$$Q_3 = N_f W_3 + 3(N_f W_2)(N_f W_1) + (N_f W_1)^3, \tag{19c}$$
$$Q_4 = N_f W_4 + 4(N_f W_3)(N_f W_1) + 3(N_f W_2)^2 + 6(N_f W_2)(N_f W_1)^2 + (N_f W_1)^4, \tag{19d}$$

and the explicit form of W_n's are given by

$$W_1 = \mathrm{tr}[B], \tag{20a}$$
$$W_2 = -\mathrm{tr}[B^2] + \mathrm{tr}[C], \tag{20b}$$
$$W_3 = 2\mathrm{tr}[B^3] - 3\mathrm{tr}[BC] + \mathrm{tr}[B], \tag{20c}$$
$$W_4 = -6\mathrm{tr}[B^4] + 12\mathrm{tr}[B^2 C] - 4\mathrm{tr}[B^2] - 3\mathrm{tr}[C^2] + \mathrm{tr}[C], \tag{20d}$$
$$B = K^{-1} \frac{\partial K}{\partial(\mu/T)}, \tag{20e}$$
$$C = K^{-1} \frac{\partial^2 K}{\partial(\mu/T)^2}, \tag{20f}$$
$$K(\mu/T) = 1 - H_0 - H_+ e^{\mu/T} - H_- e^{-\mu/T}. \tag{20g}$$

By using H_0 and $H_\pm$, one can calculate W_n and Q_n.

The Taylor expansion of the ratio of determinants is given by

$$\frac{\det D(\mu')^{N_f}}{\det D(\mu)^{N_f}} = 1 + \sum_{n=1}^{\infty} \frac{(\mu'/T - \mu/T)^n}{n!} Q_n. \tag{21}$$

Note that the Q_n are evaluated at μ. In our actual implementation, we truncate the sum at $n = 4$.

The Taylor expansion of the logarithm of the determinant ratio is given by

$$\frac{\det D(\mu')^{N_f}}{\det D(\mu)^{N_f}} = \exp\left[\sum_{n=1}^{\infty} \frac{(\mu'/T - \mu/T)^n}{n!} N_f W_n\right]. \tag{22}$$

The difference of the phase at μ and μ' is given by

$$\theta(\mu') = \theta(\mu) + \sum_{n=1}^{\infty} \frac{(\mu'/T - \mu/T)^n}{n!} \mathrm{Im} W_n. \tag{23}$$

Practically, we truncate the sum at $n = 4$.

Since the determinant is a product of eigenvalues of the Wilson-Dirac matrix whose number grows proportional to lattice volume, we expect the Taylor expansion of the logarithm of the determinant ratio to be better behaved toward larger volume than the expansion of the determinant ratio itself. We verify this explicitly in Sec. VI A in our numerical simulations.

For observables that explicitly depend on μ, e.g., quark number density and related quantities, the observables themselves also have to be evaluated at reweighted values of μ. In this study Taylor expansion is used for such observables and the details are given in Appendix B.

IV. SIMULATION PARAMETERS

In our simulations, we used the clover coefficient c_{sw} calculated from the formula

$$c_{sw} = 1 + 0.113(6/\beta) + 0.0209(6/\beta)^2 + 0.0047(6/\beta)^3. \tag{24}$$

It was nonperturbatively determined for the case of $N_f = 3$ [21]. Nevertheless, we chose it for the present exploratory study of the $N_f = 4$ case. This choice also facilitates a

TABLE I. Simulation parameters and statistics at $\beta = 1.58$ and $\kappa = 0.1385$.

$N_x N_y N_z$	$a\mu$	Acceptance	Trajectories
6^3	0.02	0.94	20000
	0.04	0.94	20000
	0.06	0.94	20000
	0.08	0.94	20000
	0.10	0.94	50000
	0.12	0.94	50000
	0.13	0.94	50000
	0.14	0.94	50000
	0.15	0.94	50000
	0.16	0.94	50000
	0.18	0.95	50000
	0.20	0.95	20000
	0.22	0.95	20000
	0.24	0.95	20000
	0.26	0.95	20000
	0.28	0.95	20000
	0.30	0.95	20000
668	0.13	0.93	50000
	0.14	0.93	50000
	0.15	0.93	50000
	0.16	0.93	50000
688	0.13	0.92	50000
	0.14	0.92	130000
	0.15	0.92	130000
	0.16	0.92	50000
8^3	0.13	0.91	275000
	0.14	0.91	275000
	0.15	0.91	275000
	0.16	0.91	50000
10^3	0.13	0.87	50000
	0.14	0.87	347800
	0.15	0.87	342800
	0.16	0.87	113900

TABLE II. Simulation parameters and statistics at $\beta = 1.60$ and $\kappa = 0.1371$.

$N_x N_y N_z$	$a\mu$	Acceptance	Trajectories
6^3	0.10	0.95	20000
	0.15	0.95	80000
	0.16	0.95	80000
	0.17	0.95	80000
	0.18	0.95	80000
	0.19	0.95	80000
	0.20	0.95	160000
	0.205	0.95	160000
	0.21	0.95	160000
	0.215	0.95	80000
	0.22	0.95	80000
	0.23	0.95	80000
	0.24	0.96	40000
	0.25	0.95	40000
	0.30	0.96	20000
	0.35	0.96	20000
668	0.205	0.94	320000
688	0.205	0.93	900000
8^3	0.10	0.93	20000
	0.15	0.92	100000
	0.16	0.92	100000
	0.17	0.92	100000
	0.18	0.92	100000
	0.19	0.92	500000
	0.20	0.92	900000
	0.205	0.92	1200000
	0.21	0.92	900000
	0.215	0.92	500000
	0.22	0.93	500000
	0.23	0.93	100000
	0.24	0.93	100000
	0.25	0.93	100000
	0.30	0.93	20000
	0.35	0.93	20000

comparison with the work of the Kentucky group [15] who adopted the same c_{sw}.

We performed nonzero-density simulations as well as zero-density ones. For the nonzero-density case, we chose two sets of parameters: $(\beta, \kappa) = (1.58, 0.1385)$ and $(1.60, 0.1371)$. The second set is exactly the same as that of the Kentucky group [15]. The spatial volume and the chemical potential are summarized in Table I for $(\beta, \kappa) = (1.58, 0.1385)$ and in Table II for $(1.60, 0.1371)$. We chose five spatial volumes, 6^3, $6^2 \times 8$, 6×8^2, 8^3 and 10^3 for finite- size scaling analyses, while fixing the temporal size to $N_t = 4$. Our control parameter for the quark number is the chemical potential, and our ensembles cover a range of $a\mu = 0.02 - 0.35$. The onset of the charged pion condensate is expected at $a\mu_c(T = 0) = am_\pi/2$. According to the hadron spectrum results summarized in Table III, we estimate $a\mu_c \approx 0.65$, and hence we do not need to worry about it in our parameter region.

For zero-density simulations, we chose two sets of parameters, $(\beta, \kappa) = (1.60, 0.1380)$ and $(1.618, 0.1371)$, and the spatial volume was varied from 6^3 to 12^3, while $N_t = 4$ was fixed for both sets. Simulation parameters are summarized in Table IV.

We used the BQCD code [22] which implements the HMC algorithm and several techniques. We used the multi-time-scale technique [23] with a ratio of step sizes of $d\tau_g$:$d\tau_d$:$d\tau_f = 1$:2:4, where $d\tau_g$, $d\tau_d$, and $d\tau_f$ are step sizes for gauge force, logarithm of determinant for clover term, and pseudofermion force, respectively. The Omelyan integrator [24] was adopted in our simulation. In order to generate a probability distribution containing the phase-quenched quark determinant, we used the finite isospin chemical potential $\mu_u = -\mu_d$. Two independent pseudofermions were employed to incorporate $N_f = 4$ dynamical quarks. We set the trajectory length to unity and fixed the step size $d\tau_f = 1/20$, with which the HMC acceptance rate stayed around 90% for all parameter sets. For each parameter set, 20,000–1,200, 000 trajectories were accumulated. The acceptance rate and the number of

TABLE III. Hadron spectrum for $N_f = 4$ QCD.

β	$N_x N_y N_z \times N_t$	κ	am_π	am_ρ	am_N
1.580	$12^3 \times 24$	0.1380	1.3666(16)	1.6550(26)	2.6529(39)
1.580	$12^3 \times 24$	0.1385	1.3317(16)	1.6197(23)	2.5745(46)
1.580	$12^3 \times 24$	0.1390	1.2896(16)	1.5830(23)	2.5108(29)
1.600	$12^3 \times 24$	0.1371	1.3958(15)	1.6639(25)	2.6473(36)
1.600	$12^3 \times 24$	0.1380	1.3275(10)	1.6097(19)	2.5790(42)
1.600	$12^3 \times 24$	0.1390	1.2392(15)	1.5340(26)	2.4170(20)
1.618	$12^3 \times 24$	0.1371	1.3497(19)	1.6166(27)	2.5521(21)
1.618	$12^3 \times 24$	0.1380	1.2686(17)	1.5465(31)	2.4810(61)
1.618	$12^3 \times 24$	0.1390	1.1511(16)	1.4240(24)	2.2651(42)

TABLE IV. Simulation parameters and statistics at $a\mu = 0$.

β	κ	$N_x N_y N_z$	Acceptance	Trajectories
1.600	0.1380	6^3	0.95	40000
		668	0.94	40000
		688	0.93	40000
		8^3	0.92	40000
		10^3	0.89	40000
		12^3	0.86	20000
1.618	0.1371	6^3	0.96	20000
		668	0.95	40000
		688	0.94	40000
		8^3	0.93	40000
		10^3	0.91	40000
		12^3	0.88	20000

trajectories were compiled in Tables I and II. The ingredients of the determinant in Eq. (20) were measured at every ten trajectories. We employed jackknife analyses with varying bin sizes and chose the maximum estimated statistical error to be quoted in this paper.

V. DEFINITION OF PHYSICAL QUANTITIES

A. Moments and cumulants

Let X be the space-time average of a local observable. In general, noncentral moments μ_n, $n = 1, 2, 3, \ldots$ and cumulants κ_n of X can be defined by the QCD partition function in the presence of source term $\mathcal{Z}_{\rm QCD}(\alpha) = \langle \exp(\alpha X) \rangle$ according to

$$\mu_n = \frac{1}{\mathcal{Z}_{\rm QCD}(\alpha)} \frac{\partial^n \mathcal{Z}_{\rm QCD}(\alpha)}{\partial \alpha^n} \bigg|_{\alpha=0} \tag{25}$$

and

$$\kappa_n = \frac{\partial^n \log \mathcal{Z}_{\rm QCD}(\alpha)}{\partial \alpha^n} \bigg|_{\alpha=0}. \tag{26}$$

If the parameter α is contained in the action, one can take the derivative without introducing the source term. This applies to the gluon action density for which α can be taken as the inverse gauge coupling β and the quark number density for which $\alpha = \mu/T$, apart from some coefficient proportional to volume.

The quantities of the most interest for our finite-size scaling analyses are susceptibility χ_X, skewness S_X, and kurtosis K_X defined, respectively, by

$$\chi_X = V\kappa_2, \tag{27}$$

$$S_X = \frac{\kappa_3}{\kappa_2^{3/2}}, \tag{28}$$

$$K_X = \frac{\kappa_4}{\kappa_2^2}. \tag{29}$$

We also analyze the Challa-Landau-Binder (CLB) cumulant [25,26]) defined in terms of noncentral moments according to

$$U_X = 1 - \frac{\mu_4}{3\mu_2^2}. \tag{30}$$

Divergence of the susceptibility peak height with volume is a well-known indicator of the nature of the transition. Both the peak of the susceptibility and the zero of the skewness $S_X = 0$ can be interpreted as the location of the transition point. Infinite volume limit of kurtosis at the transition point determined by the peak position of the susceptibility or the zero of the skewness provides a diagnosis on the nature of transition as follows:

(1) $\lim_{V\to\infty} K_X = -2$: first order,
(2) $-2 < \lim_{V\to\infty} K_X < 0$: second order with the value determined by the universality class,
(3) $\lim_{V\to\infty} K_X = 0$: crossover.

Infinite volume limit of the minimum value of the CLB cumulant is as follows:

(1) $\lim_{V\to\infty} U_X \neq 2/3$: first or second order,
(2) $\lim_{V\to\infty} U_X = 2/3$: crossover.

The reasoning for the first-order phase transition case is given in Appendix A, where the limit value of the CLB cumulant is given in terms of the expectation value of X in the two phases. Of course we do not *a priori* know these values which are dictated by dynamics. Therefore, the limit value of the CLB cumulant is not sufficient to distinguish between a first- and a second-order transition. The difference may become clear by looking at the volume scaling. For instance, if the volume scaling is given by an integer power V, then the transition is considered as first order.

B. Plaquette, gluon action density, and Polyakov loop

The plaquette average is given by

$$P = \frac{1}{18VN_t} \sum_{x, 1\le\nu<\rho\le 4} \mathrm{Re} W^{1\times 1}_{\nu\rho}, \tag{31}$$

where the individual plaquette $W^{1\times 1}_{\nu\rho}$ is defined in Eq. (6) and V denotes the spatial lattice volume $V = N_x N_y N_z$. The gauge action density is defined as

$$G = \frac{1}{6VN_t} \sum_x \Big\{ c_0 \sum_{1\le\nu<\rho\le 4} \Big(1 - \frac{1}{3}\mathrm{Re} W^{1\times 1}_{\nu\rho}(x)\Big) + c_1 \sum_{1\le\nu,\rho\le 4} \Big(1 - \frac{1}{3}\mathrm{Re} W^{1\times 2}_{\nu\rho}(x)\Big)\Big\}, \tag{32}$$

and the Polyakov loop is defined by

$$L = \frac{1}{3V} \sum_{\mathbf{x}} \mathrm{tr}\Big[\prod_{x_4=1}^{N_t} U(\mathbf{x}, x_4, \nu = 4) \Big]. \tag{33}$$

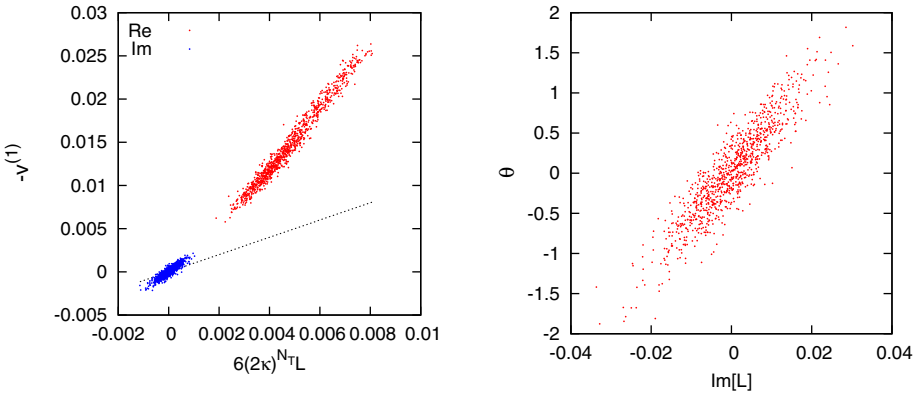

FIG. 2 (color online). (a) Correlation between the the fuzzy Polyakov loop $-v^{(1)}$ and Polyakov loop L, multiplied with $6(2\kappa)^{N_t}$ on 1000 phase-quenched configurations. Red (group of points located in the upper-right) and blue (lower-left corner) point, respectively, represent the real and imaginary parts. The dotted black line shows the static limit for the fuzzy Polyakov loop given in Eq. (37). (b) Correlation between the phase of determinant and the imaginary part of the Polyakov loop. The simulation parameters are as follows: $8^3 \times 4$, $\beta = 1.60$, $\kappa = 0.1371$ and $a\mu = 0.205$.

For the three gluonic quantities defined above, writing $X = P$, G, or L, the cumulants[1] are explicitly given by

$$\chi_X = VN_t\langle (X - \langle X\rangle)^2\rangle S_X = \frac{\langle (X - \langle X\rangle)^3\rangle}{\langle (X - \langle X\rangle)^2\rangle^{3/2}} \quad (34)$$

$$= \frac{\langle X^3\rangle - 3\langle X^2\rangle\langle X\rangle + 2\langle X\rangle^3}{(\langle X^2\rangle - \langle X\rangle^2)^{3/2}}, \quad (35)$$

$$K_X = \frac{\langle (X - \langle X\rangle)^4\rangle}{\langle (X - \langle X\rangle)^2\rangle^2} - 3 = \frac{\langle X^4\rangle - 4\langle X^3\rangle\langle X\rangle - 3\langle X^2\rangle^2 + 12\langle X^2\rangle\langle X\rangle^2 - 6\langle X\rangle^4}{(\langle X^2\rangle - \langle X\rangle^2)^2}. \quad (36)$$

Note that we include a factor N_t in the susceptibility by convention.

C. Fuzzy Polyakov loop

The quantity $v^{(q)}$ defined in the winding expansion of the determinant in Eq. (15) is a sum of gauge loops winding around the time direction q times. In this sense they define a fuzzy Polyakov loop. For example, $v^{(1)}$ turns out to be a normal Polyakov loop in the static limit up to an overall normalization,

$$v^{(1)} \overset{\kappa\to 0}{=} -(2\kappa)^{N_t} 2 \cdot 3L, \quad (37)$$

where L is the Polyakov loop in Eq. (33).

In Fig. 2(a), we show the correlation between $-v^{(1)}$ and $6(2\kappa)^{N_t}L$. The real part, as well as the imaginary part, shows a strong correlation in the parameter space where we investigate; albeit, the deviation from the static limit is significant.

As is seen from Eq. (15), the imaginary part of $v^{(q)}$ contributes to the phase of the determinant. Therefore, a correlation between the phase and the imaginary part of the Polyakov loop is also expected. It is indeed confirmed in Fig. 2(b), where the phase is exactly computed from $W(\mu/T) \in \mathbb{C}$ in Eq. (12) up to 2π periodicity. Such a correlation was observed in Ref. [27] in the heavy mass region for the staggered quark action.

If the power of fugacity is promoted to an independent parameter for each $q \in \mathbb{Z}$,

$$e^{q\mu/T} \to \lambda^{(q)}, \quad (38)$$

then $v^{(q)}$ can be considered as the first derivative of the promoted partition function $\mathcal{Z}_{\rm QCD}$ in terms of the new parameter,

$$\langle v^{(q)}\rangle = -\frac{1}{N_f V}\frac{\partial \ln \mathcal{Z}_{\rm QCD}}{\partial \lambda^{(q)}}\bigg|_{\lambda^{(q)}=\exp(q\mu/T)}, \quad (39)$$

with

$$\mathcal{Z}_{\rm QCD}(.., \lambda^{(1)}, \lambda^{(2)}, \lambda^{(3)}, \ldots) = \int [dU] \exp\{-S_G[U] + N_f \ln A_0 - N_f V \sum_{q\in\mathbb{Z}} \lambda^{(q)} v^{(q)}\}. \quad (40)$$

In the end, we impose $\lambda^{(q)} = e^{q\mu/T}$ for all $q \in \mathbb{Z}$ to restore the original theory. Singularities of the theory may be captured by this quantity. Therefore, we analyze higher cumulants of $v^{(q)}$ defined by taking higher derivatives of $\ln \mathcal{Z}_{\rm QCD}$. In practice, we exclusively analyze the cumulants of $v^{(1)}$.

[1]For the Polyakov loop susceptibility, we define $\chi_L = V\langle (L - \langle L\rangle)^2\rangle$ without a factor N_t.

D. Quark number

The quark number density normalized by T^3 is given by

$$\frac{n_q}{T^3} = \frac{1}{VT^3}\frac{\partial \ln Z_{QCD}}{\partial(\mu/T)} = \frac{\langle Q_1\rangle}{VT^3}. \quad (41)$$

Following the general definition adopted in Sec. VA, the other higher moments are given by

$$\frac{\chi_q}{T^2} = \frac{1}{VT^3}(\ln Z_{QCD})^{(2)} = \frac{\langle Q_2\rangle - \langle Q_1\rangle^2}{VT^3}, \quad (42)$$

$$S_q = \frac{(\ln Z_{QCD})^{(3)}}{((\ln Z_{QCD})^{(2)})^{3/2}} = \frac{\langle Q_3\rangle - 3\langle Q_2\rangle\langle Q_1\rangle + 2\langle Q_1\rangle^3}{(\langle Q_2\rangle - \langle Q_1\rangle^2)^{3/2}}, \quad (43)$$

$$K_q = \frac{(\ln Z_{QCD})^{(4)}}{((\ln Z_{QCD})^{(2)})^2} = \frac{\langle Q_4\rangle - 4\langle Q_3\rangle\langle Q_1\rangle - 3\langle Q_2\rangle^2 + 12\langle Q_2\rangle\langle Q_1\rangle^2 - 6\langle Q_1\rangle^4}{(\langle Q_2\rangle - \langle Q_1\rangle^2)^2}, \quad (44)$$

where (n) means the nth derivative $\partial^n/\partial(\mu/T)^n$, $Q_n(n = 1, 2, 3, 4)$ are given in Eq. (19), and the CLB cumulant takes the form

$$U_q = 1 - \frac{\langle Q_4\rangle}{3\langle Q_2\rangle^2}. \quad (45)$$

VI. SIMULATION RESULTS

We now discuss simulation results for the expectation value, susceptibility, and higher cumulants. In the figures, we only plot their real part since their imaginary part vanishes due to symmetry.

A. Numerical evaluation of μ reweighting

In Fig. 3, we compare the three expansion schemes introduced in Sec. III, taking the susceptibility of the plaquette for illustration. The starting value is $a\mu = 0.14$, and the results of μ reweighting are shown by the one standard deviation error bands. The simulation parameters are given in the figure. The performance of μ reweighting can be measured by comparison of the bands with actual measurements away from $a\mu = 0.14$ plotted by filled circles. Comparing the results for $8^3 \times 4$ lattice in (a) and for $10^3 \times 4$ lattice in (b), we see that the winding expansion works better for larger volume. The Taylor expansion develops a fake transition around $a\mu = 0.128$ on $8^3 \times 4$ lattice and around $a\mu = 0.133$ on $10^3 \times 4$ lattice, respectively. The applicable range of μ reweighting for this expansion becomes smaller for larger volumes. In contrast to the two expansions, the Taylor expansion of the logarithm is working well for both lattice sizes, and the applicable range is quite wide compared with the other expansion schemes.

A possible explanation of this behavior is as follows. As is seen from Eq. (20), the coefficients of Taylor expansion of the logarithm W_n are made of single trace whose magnitude would be proportional to the reduced space, namely the spatial lattice size $W_n \propto V$. Since this holds for all $n = 1, 2, 3, 4, \ldots$, the magnitude of W_n would not increase for larger n. Such a tendency is observed in $\langle W_n\rangle_{||}$, as shown in Fig. 4. On the other hand, the coefficients of Taylor expansion Q_n are made from a product of W_n. Hence, the dominant volume scaling is expected to be $Q_n \propto V^n$, and this tendency is seen in Fig. 4. In this way, we conclude that the Taylor expansion of the logarithm of the determinant is the best among our choices. This expansion scheme is used in the following μ-reweighting results.

Lastly, we compare μ reweighting from ensembles at three original values of μ given by $a\mu = 0.02$ and 0.14 and 0.30 in Fig. 5. The statistics for each ensemble are

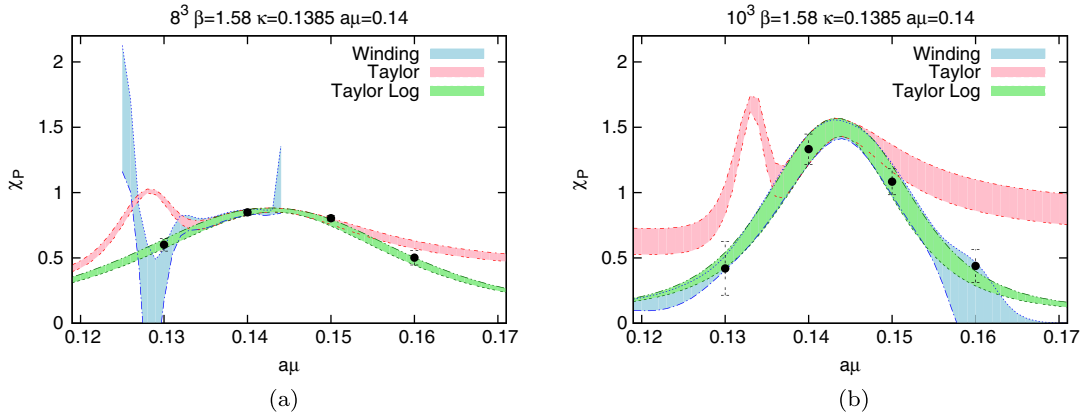

FIG. 3 (color online). Comparison of three expansion schemes of μ reweighting for the susceptibility of the plaquette. Winding expansion: blue band; Taylor expansion: red band; Taylor expansion of the logarithm of the determinant:green band. Black symbols are direct simulation data. The original μ value is $a\mu = 0.14$. (a) $8^3 \times 4$, (b) $10^3 \times 4$.

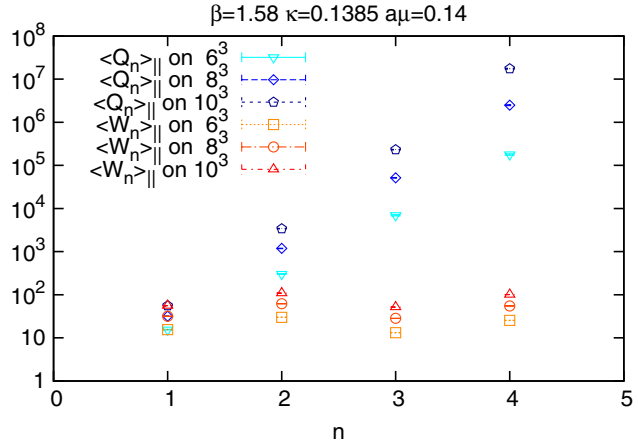

FIG. 4 (color online). Phase-quenched average of coefficients Q_n and W_n as a function of n. Q_n are for the Taylor expansion of the determinant and W_n for the Taylor expansion of the logarithm of the determinant. The spatial volume is changed from 6^3 to 10^3, while the temporal lattice size is fixed to $N_t = 4$. Error bars are too small to see at this scale.

roughly the same order. We observe that the data reweighted from $a\mu = 0.14$ show an excellent agreement with the actual simulation data plotted by filled circles over a wide range from $a\mu = 0.02$ to 0.30. Also the estimated errors do not change much over this region. On the other hand, the reweighting from $a\mu = 0.02$ and 0.30 do not work well away from the original value. This may mean that not only the truncation error of the expansion but also the overlap issue is very important. The configurations generated at $a\mu = 0.14$ are sampled from both the low-density phase and the high-density phase. Therefore, the distribution of the plaquette has large overlaps with both phases. On the other hand, the configurations generated at $a\mu = 0.02$ are mainly sampled from the low-density phase, and hence the overlap with the high-density phase region is very small. An opposite situation holds for the configurations generated at $a\mu = 0.30$.

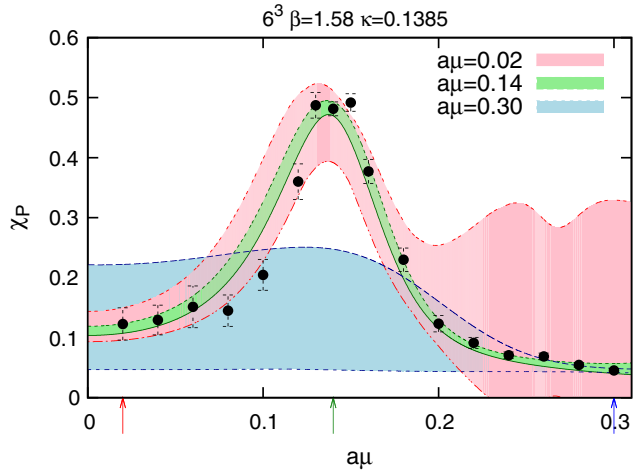

FIG. 5 (color online). Comparison of the susceptibility of the plaquette calculated from μ reweighting and from direct simulation. Black symbols show results from direct simulations. Colored regions show one standard deviation bands of μ-reweighted results. Three different ensembles are used for μ reweighting, and their respective simulation points, $a\mu$, are labeled in the figure and also pointed at the horizontal axis by the same colored arrow.

B. Phase-reweighting factor

In Fig. 6 we show the phase-quenched average of the phase-reweighting factor as a function of $a\mu$ at $\beta = 1.58$ and 1.60. The μ-reweighting one standard deviation error bands from $a\mu = 0.14$ at $\beta = 1.58$ and from $a\mu = 0.205$ at $\beta = 1.60$ are also shown. For larger volumes, the reweighting factor tends closer to zero, such that the sign problem becomes more serious as expected. However, since the phase-reweighting factor remains nonvanishing beyond statistical errors, the sign problem is under control for the lattice volumes and the parameter sets used in the present simulations.

An interesting observation is that there is a local minimum around $a\mu = 0.14$ ($a\mu = 0.2$) for $\beta = 1.58$ ($\beta = 1.60$). This is related to a change in the partition function, which usually appears as a consequence of a phase transition. It will be apparent when we discuss the behavior of the pressure in Sec. VI J.

C. Comparison between QCD and phase-quenched QCD

Figure 7 compares the average value of the plaquette and the quark number density calculated with and without the phase of the quark determinant at $\beta = 1.60$ on a $8^3 \times 4$ lattice. Apart from a small difference resembling a shift in $a\mu$ in the region of rapidly increasing plaquette, the effect of inclusion of the phase is quite small in the figure for large values of $a\mu$. Such a trend is observed also for higher moments and other physical quantities. Similar observation has been reported in Ref. [28] in $N_f = 2$ QCD by the phase-reweighting method. In Ref. [29] it was argued that such a phenomenon should hold at the parameter points outside of the charged pion condensation phase in the large N_c limit.

D. Comparision with the Kentucky group

The Kentucky group [15] carried out a canonical simulation at $\beta = 1.60$ and $\kappa = 0.1371$ on a $6^3 \times 4$ lattice employing the same gluon and quark actions as in the present study. In their work, the quark or baryon chemical potential $\mu_q = \mu_B/3$ is measured at fixed quark or baryon number $n_q = 3n_B$, and they constructed an S shape in their baryon number versus baryon chemical potential plot. In our grand canonical simulation, on the other hand, the input is the chemical potential and the output is the quark number. We numerically compare the two approaches in

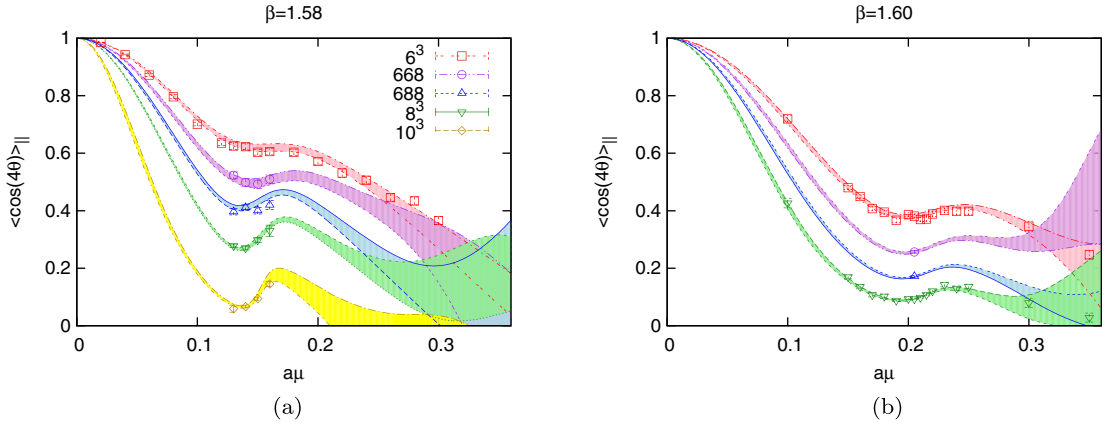

FIG. 6 (color online). The phase-reweighting factor as a function of chemical potential at (a) $\beta = 1.58$ and (b) $\beta = 1.60$. The spatial volume is changed from 6^3 to 10^3 (6^3 to 8^3) for $\beta = 1.58$ ($\beta = 1.60$). Filled curves show 1σ error band of the μ-reweighed data from the original point at $a\mu = 0.14$ and 0.205 for $\beta = 1.58$ and 1.60, respectively.

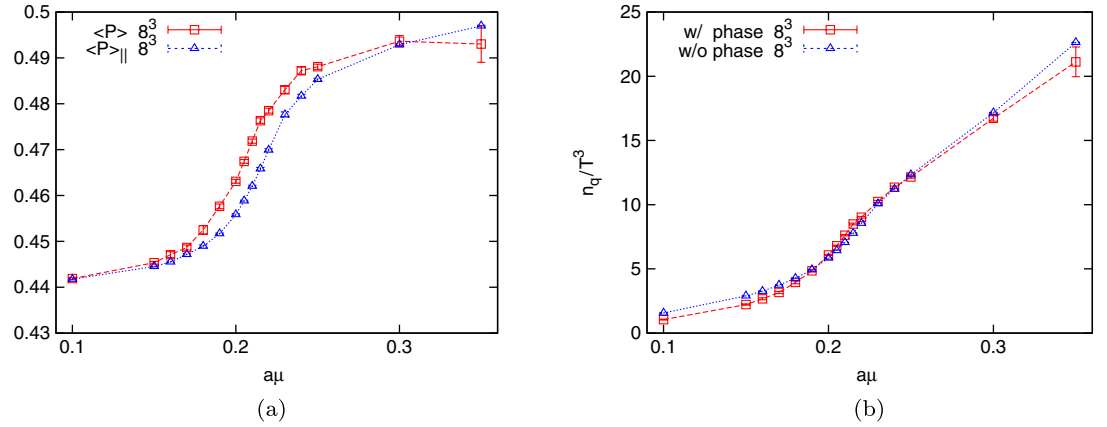

FIG. 7 (color online). (a) Plaquette average and (b) quark number density as a function of $a\mu$ at $\beta = 1.60$ on a $8^3 \times 4$ lattice. Red squares are results for full QCD and blue triangles for phase-quenched QCD.

Fig. 8 for the same parameter set; filled symbols in (a) with vertical error bars are the canonical results from Fig. 7 (bottom) in Ref. [15], whereas open symbols in (b) with horizontal error bars are our grand canonical results.

Outside the transition region, say $n_B \leq 4$ and $n_B \geq 10$, results from the two approaches agree with each other. However, the two approaches show completely different behavior around the transition region. Graphically

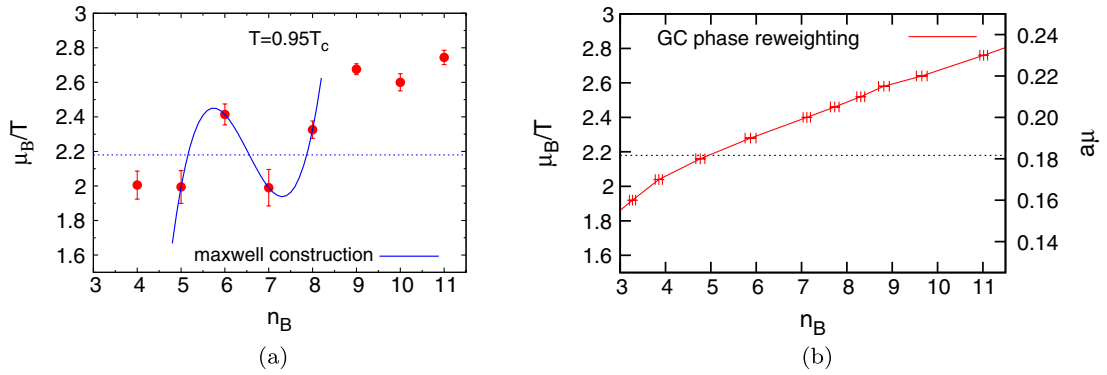

FIG. 8 (color online). Comparison of canonical [filled circles in (a)] and grand canonical [open symbols in (b)] results for the relation between baryon chemical potential μ_B/T and baryon number n_B. Canonical results are from Ref. [15] by the Kentucky group. Simulation parameters are $\beta = 1.60$, $\kappa = 0.1371$ on a lattice of size $6^3 \times 4$.

speaking in Fig. 8, while the canonical results can be made to produce an S shape presumed from a first-order transition, the grand canonical results are expected to show a smooth behavior and examination of higher cumulants such as susceptibility is required for an indication of a transition. The results of cumulant analyses, however, suggest a numerical difference: the Maxwell construction of the canonical results implies $\mu_B/T \approx 2.2$ at the transition, whereas the peak of quark number susceptibility from grand canonical results in this study takes place at $\mu_B/T \approx 2.5$. In principle, the two approaches should lead to similar results if the infinite volume limit is taken carefully.

E. Susceptibility

The susceptibility of the plaquette χ_P and quark number density χ_q/T^2 are shown in Fig. 9. We plot not only the actual simulation data with error bars but also the one standard deviation μ-reweighting band. We observe a clear volume dependence at $\beta = 1.58$; the peak grows rapidly for larger volume. At $\beta = 1.60$ the peak still grows with volume but the rate is much milder. The susceptibilities for gauge action density, Polyakov, and fuzzy Polyakov loop also show similar tendency. Therefore, it is likely that there is a phase transition at $\beta = 1.58$, while the situation at $\beta = 1.60$ requires further quantitative analyses.

We plot in Fig. 10 the volume dependence of the peak height of χ_P for (a) $\beta = 1.58$ and (b) $\beta = 1.60$. The peak position and the maximum value of χ_P are determined by the μ reweighting. The result for $\beta = 1.58$ shows a clear linear volume dependence, while that for $\beta = 1.60$ is rather weak.

To draw a quantitative conclusion, we first try a fitting of data with the functional form

$$\chi_P^{\max} = aV^b + c, \tag{46}$$

where a, b, and c are fitting parameters. It turns out that for $\beta = 1.58$, the exponent b is consistent with 1 with a reasonable error bar and reduced χ^2. On the other hand, the fit for $\beta = 1.60$ is very unstable and it is difficult to obtain a meaningful exponent. In the following, we assume a volume dependence with integer powers of V of the form

$$\chi_P^{\max} = \chi_{-1}V + \chi_0 + \chi_1/V \tag{47}$$

and consider the following three cases:

S1 setting $\chi_1 = 0$
S2 setting $\chi_{-1} = 0$
S3 no constraint.

The results of the fits are summarized in Table V for $\beta = 1.58$ and in Table VI for $\beta = 1.60$ for all susceptibilities we consider. In the bottom panels (c) and (d) in Fig. 10, the volume-scaling behavior for all physical quantities is shown together with the fitting form S3.

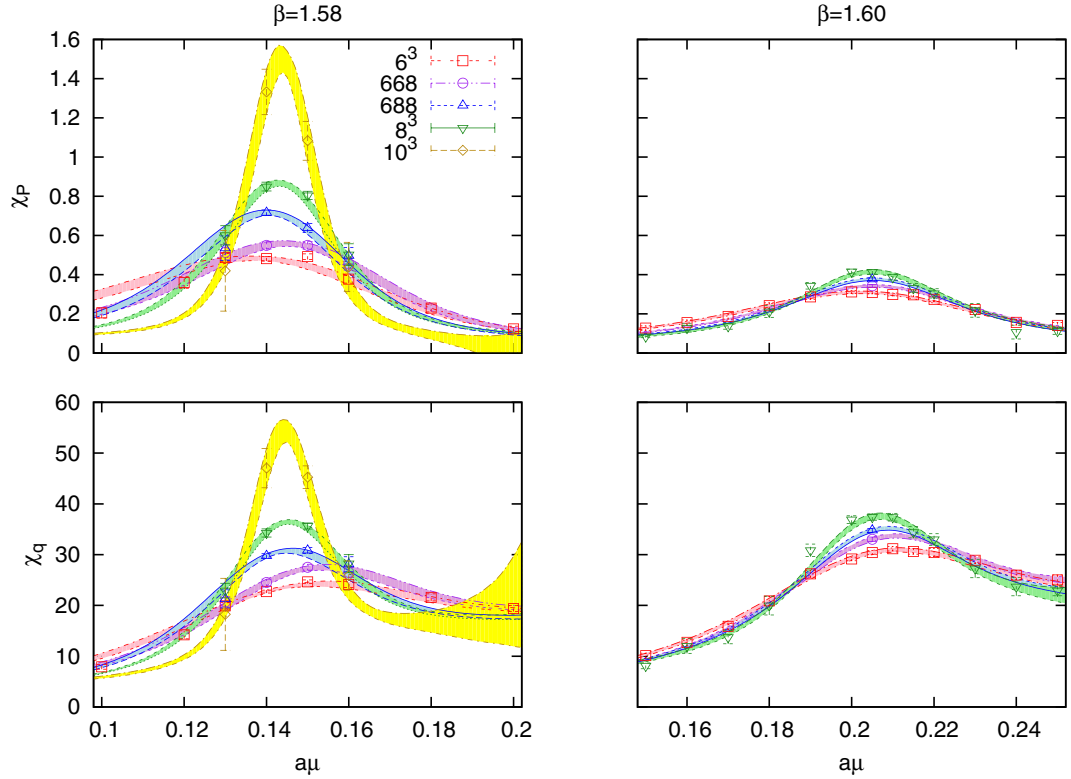

FIG. 9 (color online). Susceptibility of the plaquette (upper) χ_P and quark number density (lower) χ_q as functions of $a\mu$ at $\beta = 1.58$ (left) and $\beta = 1.60$ (right) for various spatial volumes.

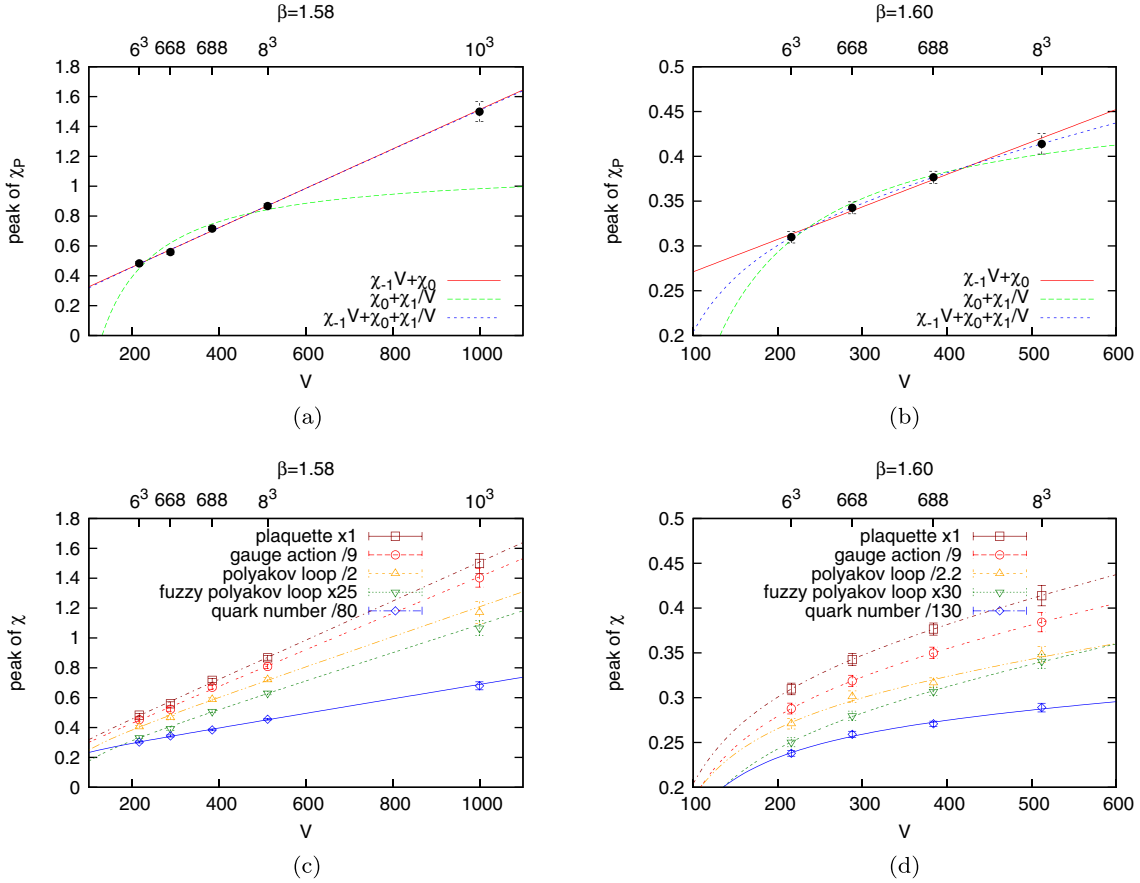

FIG. 10 (color online). Upper panels show volume scaling of the peak value of χ_P for (a) $\beta = 1.58$ and (b) 1.60 together with three types of fits. Lower panels show volume scaling plots for all observables, together with the fitting form S3 defined in the text. Vertical scales are adjusted.

Let us first look at Table V. For all five observables, the fitting form S1 exhibits a reasonable reduced χ^2, and the coefficient χ_{-1} is well determined and nonzero with less than a percent error. This situation holds even if one adds a $1/V$ term (fitting form S3), with the parameters χ_{-1} and χ_0 keeping values consistent with those from the fitting form S1. In sharp contrast, dropping the term linear in V (fitting form S2) leads to an unacceptably large reduced χ^2. We conclude that there is a first order phase transition at $\beta = 1.58$.

At $\beta = 1.60$ in Table VI, the fitting form S1 also provides a reasonable fit for all observables with a nonzero χ_{-1} at a 10% error level. However, the fitting form S2 without the term linear in volume also yields fits of similar quality. While a large negative coefficient χ_1 of the $1/V$ term in the latter fit does not seem natural, we are not able to exclude such a possibility on other grounds. With present data alone, it is difficult to draw a clear distinction between a weak but first-order phase transition and a crossover at $\beta = 1.60$. Data for a larger spatial lattice volume, e.g., 10^3, will help, but it seems very hard to accumulate enough statistics; the average of the fermion phase is already rather small for our largest spatial volume of 8^3 (see Fig. 6).

F. Skewness

The skewness of the plaquette and quark number density are shown in Fig. 11. The zero of the skewness yields an estimate of the transition point, and the slope at the zero is expected to negatively increase with volume. The latter feature is apparent in Fig. 11. The zeros estimated by μ reweighting are consistent with the peak position of the susceptibility for each observable and volume. We find the volume dependence of the position of zero to be less than 10%.

G. Kurtosis

The results of the kurtosis of the plaquette and quark number density are plotted in Fig. 12. We observe a dip that becomes sharper for larger volumes. We also find that the peak position of the susceptibility and the position of the minimum of the kurtosis are consistent with each other for all physical quantities and each volume. These features are as expected from a simple double Gaussian model discussed in Appendix A.

Figure 13 shows volume scaling of the minimum of kurtosis for all observables. At $\beta = 1.58$, the minimum decreases for larger volumes. Infinite volume extrapolations

TABLE V. Fitted values of parameters and χ^2/d.o.f. in the volume-scaling form of susceptibility in Eq. (47) for $\beta = 1.58$. Values without errors are fixed during the fit.

Observable	Fitting form	χ_{-1}	χ_0	χ_1	χ^2/d.o.f.
Plaquette	S1	0.001318(53)	0.195(19)	0	0.853
	S2	0	1.130(22)	−147.1(6.4)	31.5
	S3	0.00130(14)	0.206(99)	−2(16)	1.27
Gauge action	S1	0.01106(44)	1.65(16)	0	0.878
	S2	0	9.49(19)	−1231(53)	31.4
	S3	0.0110(11)	1.72(82)	−10(138)	1.31
Polyakov loop	S1	0.002111(94)	0.353(33)	0	0.648
	S2	0	1.816(38)	−224(11)	17.8
	S3	0.00199(28)	0.44(19)	−14(31)	0.866
Fuzzy Polyakov loop	S1	0.0000400(14)	0.00466(48)	0	0.997
	S2	0	0.03258(59)	−4.29(16)	30.3
	S3	0.0000370(39)	0.0069(28)	−0.36(44)	1.18
Quark number	S1	0.0399(19)	15.74(74)	0	0.488
	S2	0	45.04(75)	−4785(241)	23.5
	S3	0.0384(46)	17.0(3.5)	−216(600)	0.668

assuming polynomials in $1/V$, however, do not yield values close to -2 expected for a first-order phase transition. For $\beta = 1.60$, the minimum shows only weak volume dependence and even increases slightly for larger volumes.

Since kurtosis is composed of the fourth-order cumulants, statistical errors are significantly larger compared to the second-order cumulants (compare Figs. 9 and 12). Furthermore, the curvature at the minimum is expected to increase quadratically in V. Unless data at the original value is precise, μ reweighting may find a hard time estimating the bottom of a sharp valley. We feel that these features make kurtosis a rather difficult quantity. We will need much more detailed analysis with larger statistics and/or finer points of simulations to draw definitive information from kurtosis.

H. CLB cumulant

In Fig. 14, we show the CLB cumulant for the plaquette U_P, quark number density U_q, and Polyakov loop U_L. Both U_P and U_L show a unique minimum in the region we investigate. The volume dependence of the minimum position is rather large for U_L, while it is small for U_P. The results for gauge action density and fuzzy Polyakov loop show similar trends to that of the plaquette and Polyakov loop, respectively. In contrast, U_q exhibits a broad minimum even for relatively large volumes, and there is an

TABLE VI. Fitted values of parameters and χ^2/d.o.f. in the volume scaling form of susceptibility for $\beta = 1.60$.

Observable	Fitting form	χ_{-1}	χ_0	χ_1	χ^2/d.o.f.
Plaquette	S1	0.000362(39)	0.235(13)	0	0.497
	S2	0	0.472(14)	−35.8(3.9)	1.02
	S3	0.00022(15)	0.332(99)	−15(15)	0.00052
Gauge action	S1	0.00302(33)	1.97(11)	0	0.546
	S2	0	3.95(12)	−299(33)	0.924
	S3	0.0017(13)	2.83(82)	−132(127)	7.32×10^{-7}
Polyakov loop	S1	0.000555(72)	0.486(25)	0	1.03
	S2	0	0.855(25)	−56.4(7.3)	1.07
	S3	0.00029(28)	0.67(18)	−28(28)	1.08
Fuzzy Polyakov loop	S1	0.00001028(95)	0.00624(32)	0	0.714
	S2	0	0.01303(33)	−1.034(96)	1.47
	S3	0.0000062(36)	0.0090(24)	−0.43(37)	0.0651
Quark number	S1	0.0222(23)	26.63(79)	0	2.12
	S2	0	41.49(81)	−2286(235)	0.801
	S3	0.0067(89)	37.1(5.9)	−1625(909)	1.03

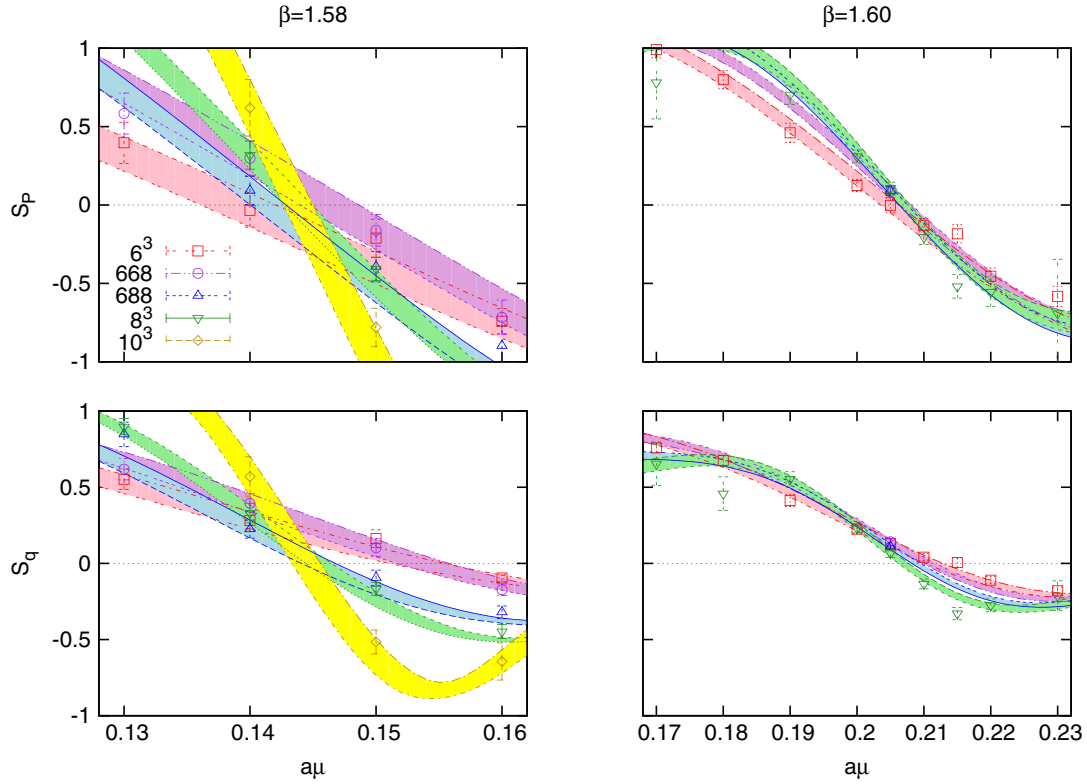

FIG. 11 (color online). Skewness of plaquette S_P (upper panels), and quark number density S_q (lower panels) as functions of $a\mu$ at $\beta = 1.58$ (left) and $\beta = 1.60$ (right).

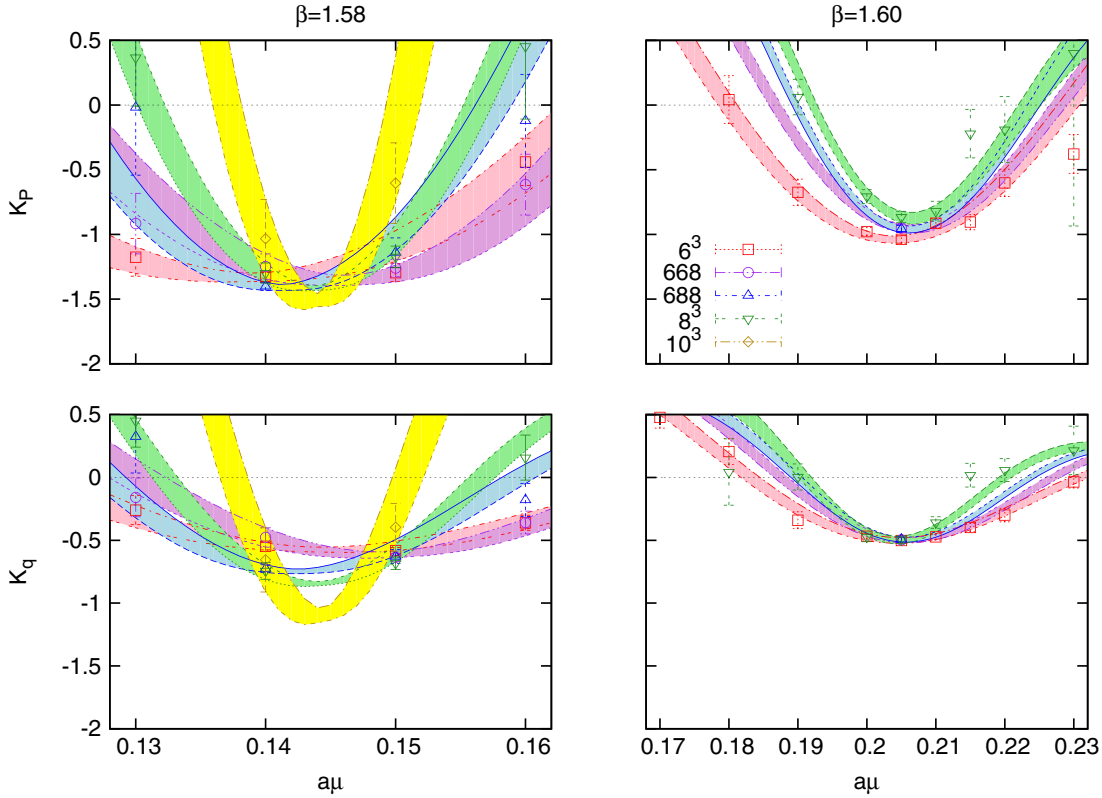

FIG. 12 (color online). Kurtosis of plaquette K_P (upper panels) and quark number density K_q (lower panels) as functions of $a\mu$ at $\beta = 1.58$ (left) and $\beta = 1.60$ (right).

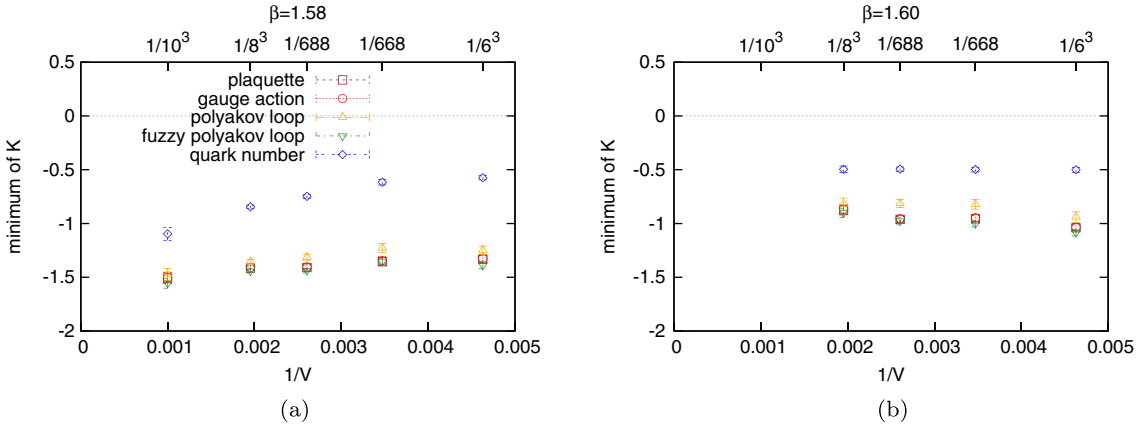

FIG. 13 (color online). Volume scaling of the minimum value of the kurtosis for all physical quantities at (a) $\beta = 1.58$ and (b) $\beta = 1.60$.

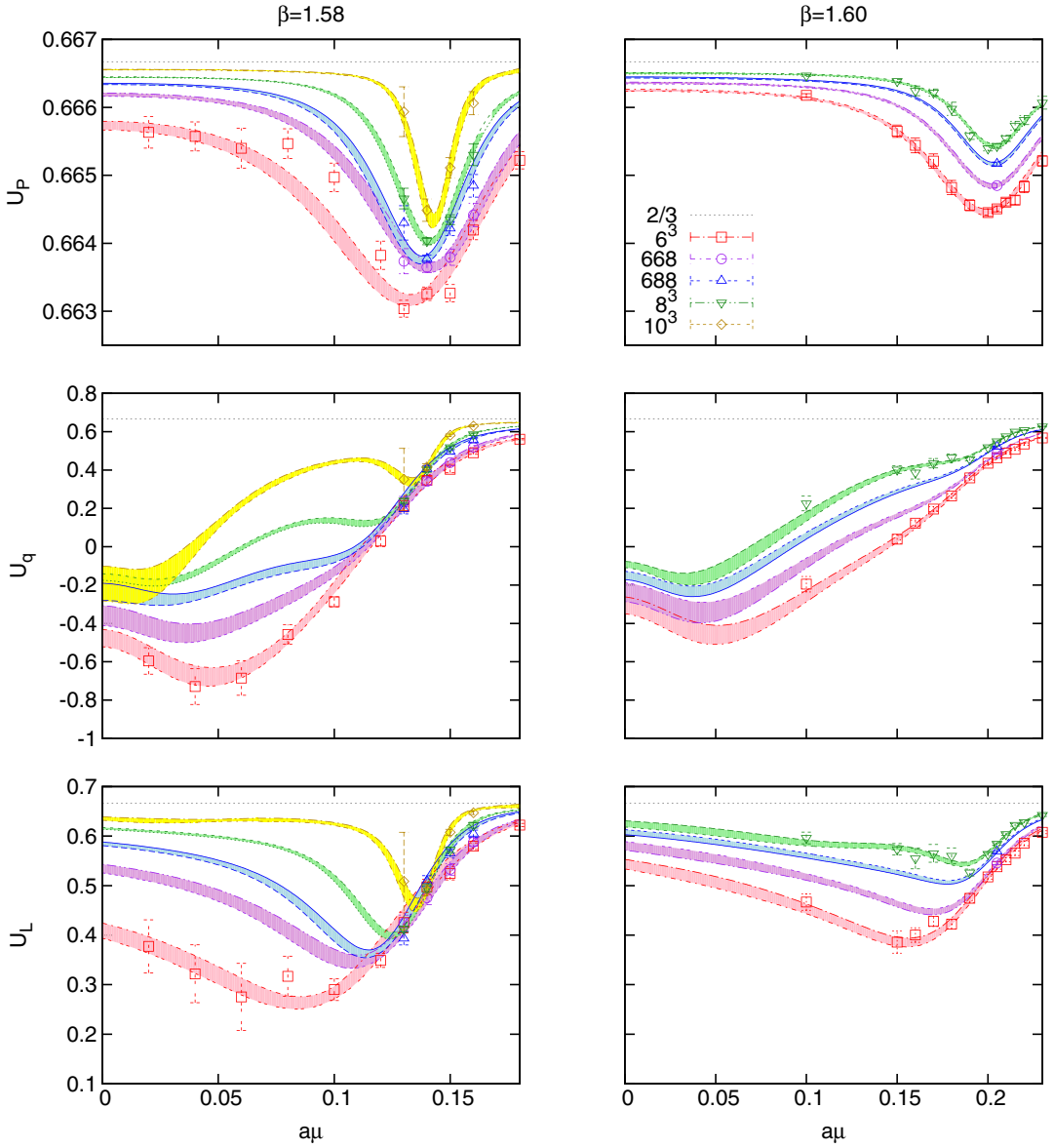

FIG. 14 (color online). CLB cumulant of the plaquette U_P (top panels), quark number density U_q (middle panels), and the Polyakov loop U_L (bottom panels) as functions of $a\mu$ at $\beta = 1.58$ (left) and $\beta = 1.60$ (right).

additional minimum generated far away from the transition region for large volumes. Since the CLB cumulant is defined in terms of noncentral moments, it may depend more on the detailed form of observable distributions than those defined in terms of central moments and their ratios. In any case, we need more understanding on the behavior of U_q, and we choose not to perform the volume-scaling analysis for U_q in the following.

In order to extract the infinite volume limit, we perform fitting with the form

$$U_P^{\min} = u_0(1 - u_1/V + u_2/V^2) \tag{48}$$

and consider the following three cases:

C1 assuming $u_2 = 0$

C2 assuming $u_0 = 2/3$

C3 no constraint.

The results for fit parameters are summarized in Tables VII and VIII for $\beta = 1.58$ and 1.60, respectively. In Fig. 15, the top panels shows the volume dependence of the minimum value of the CLB cumulant for the plaquette, together with the curves of the three fits. The bottoms panels summarize the minimum values for all observables we consider and the fit curves from the fitting form C3.

We find the results of fits to be essentially the same in character to those for the susceptibilities. At $\beta = 1.58$, data are well described by either the fitting form C1 or C3, with consistent values of the fit parameters. In particular, u_0 clearly deviates away from $2/3$. On the other hand, the fitting form C2 with u_0 fixed at $2/3$ has an unacceptably large χ^2. Thus a crossover is strongly excluded. At $\beta = 1.60$, the fitting forms C1 and C2 are equally reasonable. It is difficult to distinguish between a first-order phase transition and a crossover from present data alone.

I. Transition point

The transition point can be determined by the peak of the susceptibility or the zero of the skewness for each volume. The transition point in the infinite volume may then be obtained by a volume extrapolation with a fitting form

TABLE VII. Values of fit parameters of volume scaling form for CLB cumulant in Eq. (48) at $\beta = 1.58$. Values without error means that the corresponding parameter is fixed.

Observable	Fitting form	u_0	u_1	u_2	χ^2/d.o.f.
Plaquette	C1	0.664614(82)	0.462(44)	0	1.02
	C2	2/3	2.640(52)	342(15)	31.7
	C3	0.66463(21)	0.48(23)	4(38)	1.53
Gauge action	C1	0.664901(74)	0.398(40)	0	0.742
	C2	2/3	2.258(46)	291(13)	26.3
	C3	0.66492(20)	0.42(22)	4(35)	1.11
Polyakov loop	C1	0.499(12)	100.3(6.6)	0	1.39
	C2	2/3	255.6(7.4)	$0.296(22) \times 10^5$	10
	C3	0.511(30)	116(37)	$0.30(71) \times 10^4$	2
Fuzzy Polyakov loop	C1	0.435(16)	153.5(8.3)	0	2
	C2	2/3	353(10)	$0.403(29) \times 10^5$	12.1
	C3	0.455(38)	182(47)	$0.61(99) \times 10^4$	2.83

TABLE VIII. Values of fit parameters of volume scaling form for CLB cumulant at $\beta = 1.60$.

Observable	Fitting form	u_0	u_1	u_2	χ^2/d.o.f.
Plaquette	C1	0.666118(60)	0.545(30)	0	0.453
	C2	2/3	1.083(32)	81.2(8.9)	1.05
	C3	0.66633(23)	0.76(23)	33(35)	0.00105
Gauge action	C1	0.666175(54)	0.478(27)	0	0.573
	C2	2/3	0.961(29)	73.0(8)	0.869
	C3	0.66639(21)	0.69(20)	33(31)	1.02×10^{-5}
Polyakov loop	C1	0.6621(91)	91.3(3.7)	0	0.551
	C2	2/3	95.4(4.8)	$0.08(15) \times 10^4$	0.545
	C3	0.666(34)	95(30)	$0.06(54) \times 10^4$	1.09
Fuzzy Polyakov loop	C1	0.656(11)	117.2(4)	0	0.164
	C2	2/3	125.5(5.6)	$0.15(17) \times 10^4$	0.234
	C3	0.651(39)	112(34)	$-0.10(65) \times 10^4$	0.306

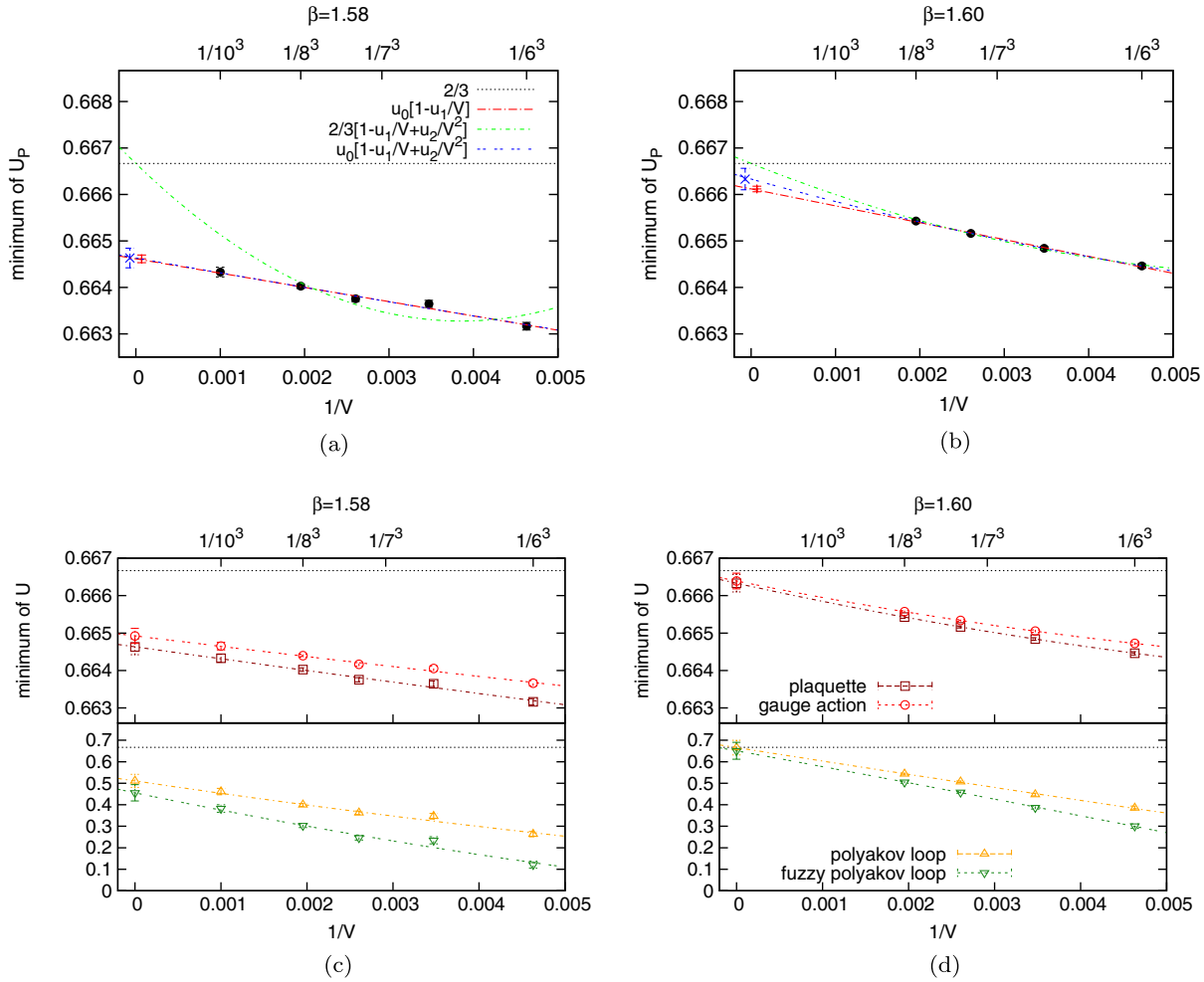

FIG. 15 (color online). Upper panels show volume scaling of the minimum of U_P for $\beta = 1.58$ (left panel) and 1.60 (right panel) together with results of three types of fits. Lower panels show volume scaling plot for the plaquette, gauge action density, Polyakov loop, and fuzzy Polyakov loop, together with results of the fitting form C3.

$$a\mu_t(V) = a\mu_t(V = \infty) + A/V, \tag{49}$$

where $a\mu_t(V = \infty)$ and A are fitting parameters. The volume dependence of the transition point determined from the susceptibility for five observables, and the volume extrapolation using Eq. (49), are shown in Fig. 16. The largest three volumes are used for the fits, namely $V = 688, 8^3, 10^3$ for $\beta = 1.58$ and $V = 668, 688, 8^3$ for $\beta = 1.60$. The transition points determined from several observables are different from each other at finite volumes. However, after taking the infinite volume limit, they coincide with each other within the estimated errors. The transition point determined by the zero of skewness gives the same value within error at each finite volume, and the final value and the size of error are similar to those calculated from susceptibilities. For future reference we quote the transition point determined from the susceptibility of the plaquette

$$a\mu_t(V = \infty) = \begin{cases} 0.1459(20) & \text{for } \beta = 1.58, \\ 0.2053(21) & \text{for } \beta = 1.60. \end{cases} \tag{50}$$

J. Pressure

For the grand canonical ensemble approach, the pressure is given by the corresponding partition function,

$$p_{\mathrm{QCD}}(\mu) = \frac{T}{V} \ln Z_{\mathrm{QCD}}(\mu). \tag{51}$$

The ratio of two partition functions is thus directly related to their difference in pressure. The averaged phase-reweighting factor, which is the ratio of full QCD partition function and phase-quenched partition function, can be expressed as the difference in pressure,

$$\begin{aligned} \langle \cos(4\theta) \rangle_{||} &= \exp\left[\frac{V}{T}(p_{\mathrm{QCD}}(\mu) - p_{\mathrm{QCD}_{||}}(\mu))\right] \\ &= \exp\left[\frac{V}{T}\Delta p(\mu)\right] \leq 1. \end{aligned} \tag{52}$$

Conversely, the pressure difference between full QCD and phase-quenched is given by $T/V \ln \langle \cos(4\theta) \rangle_{||}$ and is shown in Fig. 17(a). This can be compared with Fig. 6,

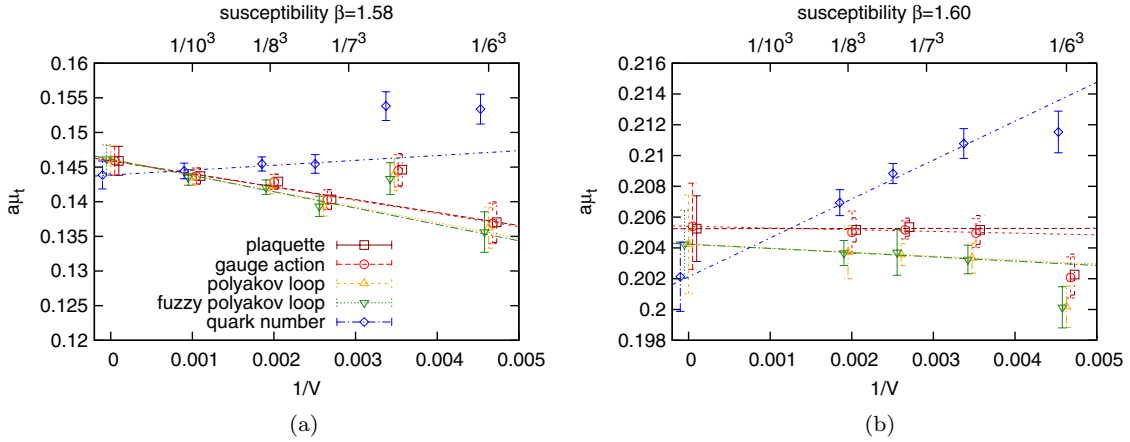

FIG. 16 (color online). Volume dependence of the transition point $a\mu_t$ determined from susceptibility peak of several observables for (a) $\beta = 1.58$ and (b) 1.60 together with the fitted line of Eq. (49).

where the dip in the phase-reweighting factor manifests itself as the dip in the pressure difference. In order to better understand the local minimum, we compare the pressure from full QCD and phase-quenched directly by plotting them together in Fig. 17(b). In this figure, we show the value of each pressure at chemical potential, μ, relative to the value at $\mu = 0$. These are computed by numerically integrating the quark number density [Eq. (41)],

$$p(\mu) - p(0) = \frac{T}{V}\int_0^{\mu} d\mu' \frac{\partial \ln \mathcal{Z}(\mu')}{\partial \mu'}, \tag{53}$$

$$= \int_0^{\mu} d\mu' n_q(\mu'). \tag{54}$$

We can see, in Fig. 17, that there is a change of slope in full QCD that appears at a relatively smaller chemical potential than the change of slope in phase-quenched QCD. This produces the dip.

The slope in figures of pressure versus chemical potential is quark number density as given in Eq. (54). The rapid increase of slope here is the same as a rapid increase of quark number density, which is an expected behavior for a phase transition. Figure 18 shows results of relative pressure in full QCD from our simulations. Compared to our moment analysis, at $\beta = 1.58$, where the first-order phase transition is suggested, the slope around the transition point ($a\mu \approx 0.146$) changes more rapidly with larger volumes, and it is likely to develop a discontinuity in the first derivative of pressure in the infinite volume limit, which is a classical signal of a first-order phase transition. On the other hand, at $\beta = 1.60$ with the volumes we have simulated, the change is less sharp, which is consistent with results from other moments, namely a crossover.

Finally, after understanding the meaning of the first derivative of pressure, the dip in Fig. 17(a) can be explained in the following way. It appears when the first derivative of pressure in full QCD changes more rapidly than that in phase-quenched. When the phase-quenched

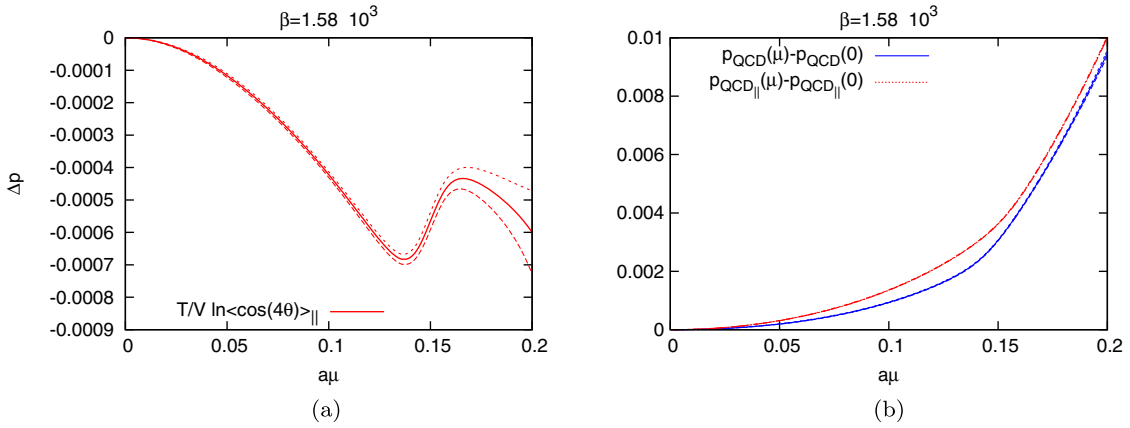

FIG. 17 (color online). The left figure is the difference of the pressure between full QCD and phase-quenched QCD with 1σ error band. The right figure is the subtracted pressure for QCD and phase-quenched QCD as a function of $a\mu$ at $\beta = 1.58$ on 10^3 lattice. The inequality $p_{\mathrm{QCD}}(\mu) \leq p_{\mathrm{QCD}_{||}}(\mu)$ in the shown range of μ is seen. The pressure here is in lattice unit.

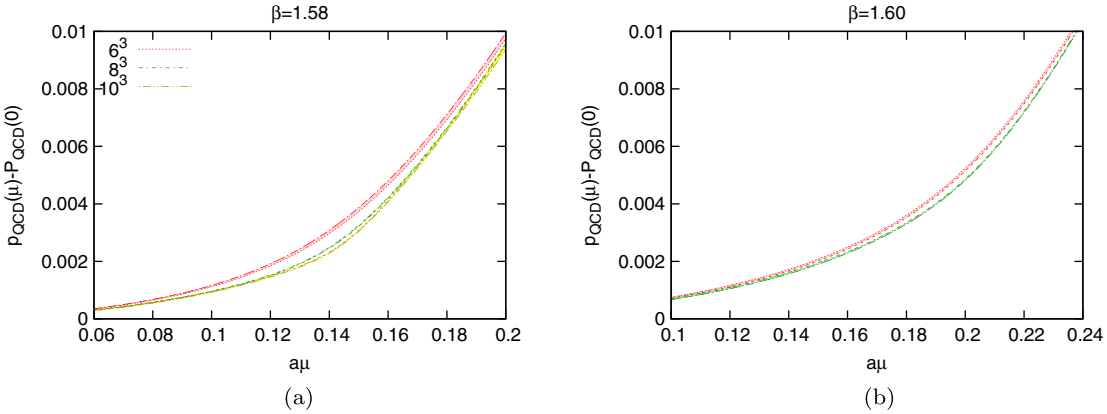

FIG. 18 (color online). The left (right) figure is the subtracted pressure as a function of $a\mu$ at $\beta = 1.58$ (1.60). The band shown here is 1 σ band.

system is away from a transition while the full QCD system undergoes a transition, such a dip becomes sharper. The dip becomes a downward wedge—a discontinuity in slope—in the thermodynamic limit, when a first-order transition occurs.

VII. GLOBAL PICTURE OF PHASE DIARGRAM

We may ask what the present results can tell us about the phase diagram depicted in Fig. 1. To answer this we made additional simulations at $a\mu = 0$ with $\kappa = 0.1380$ and 0.1371, while varying β to search for transition points. Figures 19(a) and 19(b) show the susceptibility and the CLB cumulant of the gauge action density along with the β-reweighting results (See [30] for technical details). At the transition point where susceptibilities peak, shown in Figs. 19(c)–19(f), the volume scaling of susceptibilities and CLB cumulants indicates a clear first-order phase transition at $\kappa = 0.1380$ and a much weaker transition at $\kappa = 0.1371$. Similar to finite density, linear fits to plaquette susceptibility peaks as a function of the inverse volume extrapolate transition points at

$$(\beta, \kappa, a\mu) = \begin{cases} (1.59997(11), 0.1380, 0) & \text{strong first-order phase transition (open square),} \\ (1.61848(12), 0.1371, 0) & \text{very weak first-order (open diamond).} \end{cases} \quad (55)$$

The phase diagram, Fig. 20, shows the zero-density transition line, which linearly connects the two transition points, along with the transition points at finite densities determined in Eq. (50),

$$(\beta, \kappa, a\mu) = \begin{cases} (1.58, 0.1385, 0.1459(20)) & \text{strong first-order phase transition (filled square),} \\ (1.60, 0.1371, 0.2053(21)) & \text{very weak first-order/crossover (filled diamond).} \end{cases} \quad (56)$$

At zero density, along the transition line, continuity suggests that a strong first-order transition at stronger couplings (lower-right corner of the figure) weakens toward weaker couplings (upper-left corner). To understand the phase diagram related to finite densities in terms of physical observables, we calculate m_π/m_ρ from Table III, and linearly interpolate lines of constant m_π/m_ρ. We pick specifically $m_\pi/m_\rho = 0.822$ and 0.839, evaluated at the transition points at finite densities, and show these two lines in the figure as green and magenta lines, respectively. A crossing point of such a constant m_π/m_ρ line and the zero-density transition line (black) gives us an estimate of the location of the zero-density thermal transition at the value of m_π/m_ρ, which in turn tells us the relative strength of the transition there.

In Fig. 20, at the intersection of the black and green lines, which has a stronger coupling than our simulated point (open square) at zero density, we expect a strong first-order transition, which continues to $a\mu = 0.1459(20)$ (filled square) for the system with $m_\pi/m_\rho = 0.822(2)$ along the green line. Therefore, the phase diagram for $m_\pi/m_\rho = 0.822(2)$ looks like Fig. 1(a).

On the other hand, for the system with a slightly larger pi-rho ratio $m_\pi/m_\rho = 0.839(2)$, we have argued that it has either a weak first-order transition or a quick crossover at $a\mu = 0.2053(21)$ (filled diamond). Extending toward the zero-density (black) line, the system appears at much weaker coupling than our simulated weak transition point (open diamond) and is likely to have an even weaker transition or a quick crossover. The phase diagram for

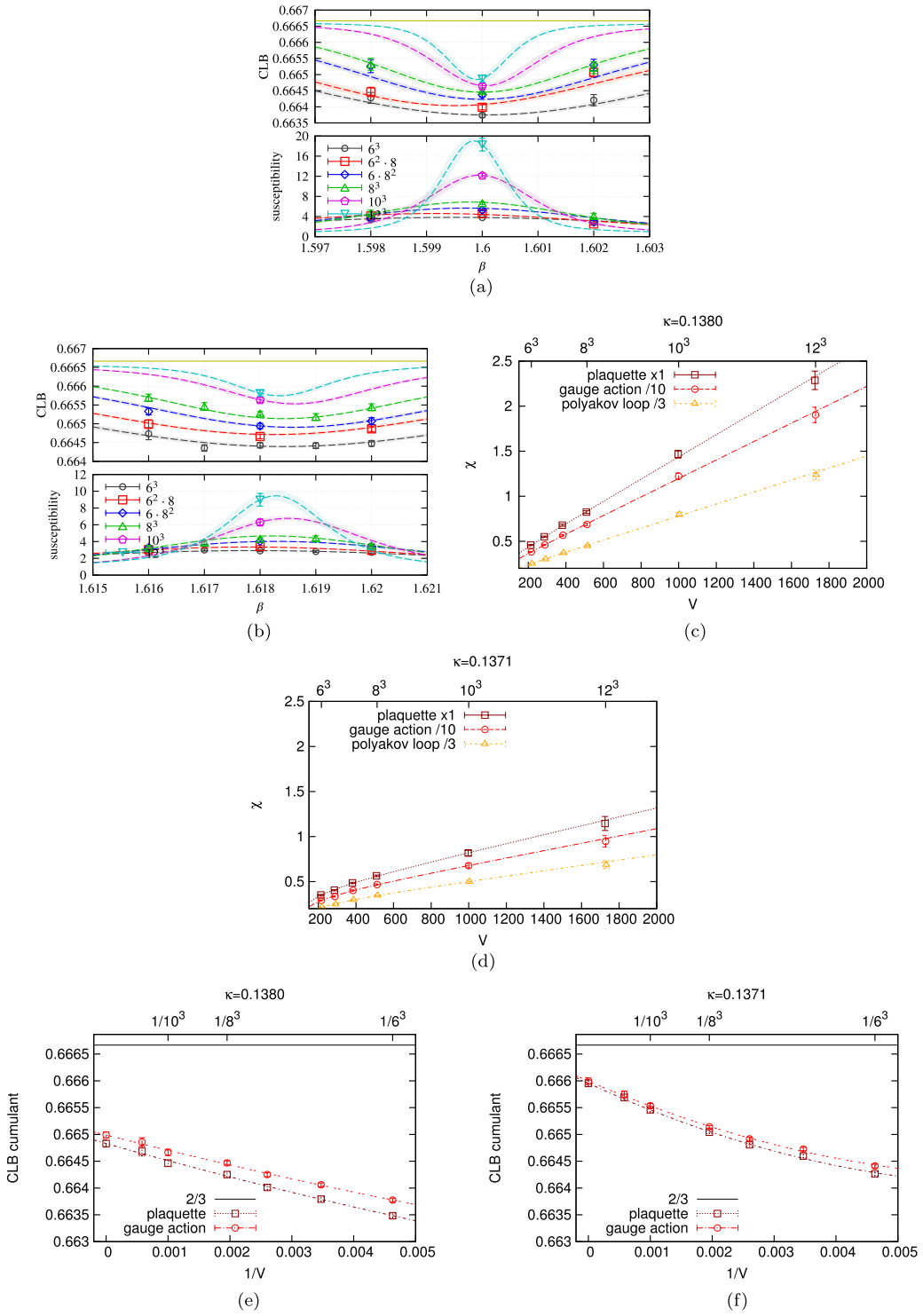

FIG. 19 (color online). The top figures are the suscepbility and the CLB cumulant of the gauge action density together with β-reweighting 1 σ band. The left figures are for $\kappa = 0.1380$, while the right figures are for $\kappa = 0.1371$. The middle and the bottom figures show the volume scaling of susceptibility and the CLB cumulant at the transition point, respectively, for the plaquette, the gauge action density, and the Polyakov loop. In the bottom figures, the CLB cumulant of the Polyakov loop is not shown because its minimum is quite far from the simulation point. The curves show the fitting forms S3 and C3, defined in the Sec. VI.

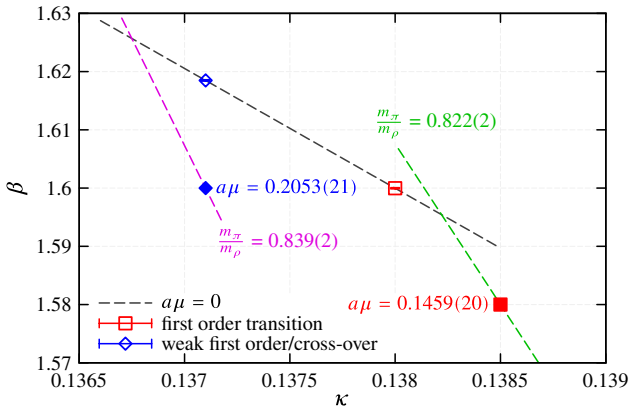

FIG. 20 (color online). The phase diagram in the bare parameter space. The black line is the transition line at zero density.

$m_\pi/m_\rho = 0.839(2)$ is, therefore, possibly consistent with Fig. 1(b).

VIII. CONCLUDING REMARKS

Taken together, the results of our finite-size scaling analyses show that there is a first-order phase transition at $\beta = 1.58$, $\kappa = 0.1385$, and $a\mu = 0.1459(20)$. On the other hand, for the Kentucky group's parameter set $\beta = 1.60$, $\kappa = 0.1371$, our range of lattice sizes from 6^3 to 8^3 is not large enough to draw a clear conclusion about the nature of the transition, although we have confirmed that the transition point $a\mu_t \approx 0.2053(21)$ is very close to that determined by their canonical approach.

Together with additional zero-density simulations, we come to the conclusion that for $m_\pi/m_\rho = 0.822(2)$ the phase diagram looks like Fig. 1(a). On the other hand, $m_\pi/m_\rho = 0.839(2)$ indicates that the transition is either a weak first- order or a crossover, and there is a possibility that the phase diagram looks like the small density region of Fig. 1(b).

ACKNOWLEDGMENTS

The authors gratefully acknowledge the useful conversation with Mike Endress, Sinya Aoki, Kazuyuki Kanaya, and Shinji Ejiri. This work is supported in part by the Grants-in-Aid for Scientific Research from the Ministry of Education, Culture, Sports, Science and Technology (No. 23105707, No. 23740177, No. 22244018, No. 20105002). The numerical calculations have been done on T2K-Tsukuba and HA-PACS cluster system at the University of Tsukuba. We thank the Galileo Galilei Institute for Theoretical Physics for the hospitality and INFN for partial support offered to S. T. during the workshop "New Frontiers in Lattice Gauge Theories," while this work was completed.

APPENDIX A: VOLUME SCALING OF HIGHER MOMENTS IN A DOUBLE GAUSSIAN MODEL

In this appendix, we summarize a phenomenological distribution argument originally due to Ref. [26]. Close to a first-order transition point, the distribution of an observable X can be approximately described by a double Gaussian form given by

$$P(X) = a_+\sqrt{\frac{V}{2\pi c_+}}e^{-\frac{(X-x_+)^2}{2c_+/V}} + a_-\sqrt{\frac{V}{2\pi c_-}}e^{-\frac{(X-x_-)^2}{2c_-/V}}. \quad \text{(A1)}$$

This distribution is normalized,

$$\int_{-\infty}^{\infty} P(X)dX = 1, \quad \text{(A2)}$$

provided $a_+ + a_- = 1$. Any observable $f(X)$ of X can be calculated as

$$\langle f(X)\rangle = \int_{-\infty}^{\infty} \mathrm{d}X f(X)P(X). \quad \text{(A3)}$$

Let t be the parameter controlling the phase transition, e.g., temperature, and let $a_+ = a_- = 1/2$ or $t = 0$ be the transition point at infinite volume. The infinite volume free-energy density has two branches that cross at $t = 0$ and switches the minimum. Normalizing the scale of t, one can write

$$a_\pm = \frac{e^{\pm Vt}}{e^{Vt} + e^{-Vt}}. \quad \text{(A4)}$$

Simple but tedious calculation leads to the following expressions for the susceptibility, skewness, kurtosis, and the CLB cumulant:

$$\begin{aligned}\chi_X &= V\langle (X - \langle X\rangle)^2\rangle \\ &= Va_+a_-(x_+ - x_-)^2 + (a_+c_+ + a_-c_-),\end{aligned} \quad \text{(A5)}$$

$$S_X = \frac{\langle (X - \langle X\rangle)^3\rangle}{\langle (X - \langle X\rangle)^2\rangle^{3/2}} = -\frac{a_+ - a_-}{\sqrt{a_+a_-}} + O(V^{-1}), \quad \text{(A6)}$$

$$K_X = \frac{\langle (X - \langle X\rangle)^4\rangle}{\langle (X - \langle X\rangle)^2\rangle^2} - 3 = -2 + \frac{1 - 4a_+a_-}{a_+a_-} + O(V^{-1}), \quad \text{(A7)}$$

$$U_X = 1 - \frac{1}{3}\frac{\langle X^4\rangle}{\langle X^2\rangle^2} = \frac{2}{3} - \frac{a_+a_-(x_+^2 - x_-^2)^2}{3(a_+x_+^2 + a_-x_-^2)^2} + O(V^{-1}). \quad \text{(A8)}$$

Another simple calculation of derivative with respect to t leads to

$$\frac{d\chi_X}{dt} = -b(a_+ - a_-)(x_+ - x_-)^2V^2 + b(c_+ - c_-)V, \quad \text{(A9)}$$

$$\frac{dS_X}{dt} = -\frac{b}{2(a_+a_-)^{3/2}}V + O(V^0), \tag{A10}$$

$$\frac{dK_X}{dt} = -b\frac{a_+ - a_-}{(a_+a_-)^2}V + O(V^0), \tag{A11}$$

$$\frac{dU_X}{dt} = \frac{b}{3}\frac{(a_+x_+^2 - a_-x_-^2)}{(a_+x_+^2 + a_-x_-^2)^3}(x_+^2 - x_-^2)^2V + O(V^0), \tag{A12}$$

with $b = 2/(e^{Vt} + e^{-Vt})$.

From the above equations, we read that the peak of susceptibility, zero of skewness, and minimum of kurtosis take place at the same value $t = 0$ up to corrections of $O(V^{-2})$. Expanding the skewness and kurtosis in the leading orders of V around $t = 0$ with $Vt \ll 1$, we find

$$S_X = -2Vt + O(V^0), \tag{A13}$$

$$K_X = -2 + 4V^2t^2 + O(V^1). \tag{A14}$$

Therefore, in the leading order, the slope of skewness increases linearly, and the curvature of kurtosis quadratically, with volume.

The CLB cumulant exhibits a subtlety. The minimum position deviates from $t = 0$ by $O(V^{-1})$,

$$t_{\mathrm{CLB\,min}} = \frac{1}{2V}\ln\frac{x_-^2}{x_+^2} + O(V^{-2}). \tag{A15}$$

The infinite volume values at this minimum and at $t = 0$ differ,

$$U_X|_{t=t_{\mathrm{CLB\,min}}} = \frac{2}{3} - \frac{(x_+^2 - x_-^2)^2}{12x_+^2x_-^2} + O(V^{-1}), \tag{A16}$$

$$U_X|_{t=0} = \frac{2}{3} - \frac{(x_+^2 - x_-^2)^2}{3(x_+^2 + x_-^2)^2} + O(V^{-1}). \tag{A17}$$

It may seem paradoxical that $\lim_{V\to\infty} t_{\mathrm{CLB\,min}} = 0$, while $\lim_{V\to\infty} U_X|_{t=t_{\mathrm{CLB\,min}}} \neq U_X|_{t=0}$. This is because, at the minimum of the CLB cumulant, $\lim_{V\to\infty}\frac{a_+}{a_-} = \frac{x_-^2}{x_+^2}$, which is away from unity where the phase transition occurs even in the infinite volume limit.

APPENDIX B: REMARK ON μ REWEIGHTING FOR QUARK NUMBER–RELATED QUANTITIES

Note that the observables, like plaquette value, gauge action, Polyakov loop, and fuzzy Polyakov loop, are independent of μ, while the quark number density has an explicit μ dependence. Therefore, we have to identify a difference in the observable,

$$\mathcal{O}(\mu') = \mathcal{O}(\mu) + \Delta\mathcal{O}(\mu', \mu). \tag{B1}$$

Before identifying the difference, first let us note the quark number–related quantities. Actually, they can be expressed by using Q_n in Eq. (19) as follows. In order to construct the quark number–related observable at μ', we have to know $Q_n(\mu')$. For that purpose, we have to know $W_n(\mu'/T)$ as seen from Eq. (19),

$$W_n(\mu'/T) = W_n(\mu/T) + \Delta W_n(\mu'/T, \mu/T). \tag{B2}$$

There are two ways to approximate $\Delta W_n(\mu'/T)$, namely, the winding expansion and the Taylor expansion. In the following we show only the latter, and it is given by

$$W_n(\mu'/T) = \sum_{m=0}^{\infty}\frac{(\mu'/T - \mu/T)^m}{m!}\frac{\partial^m W_n(\mu/T)}{\partial(\mu/T)^m} = \sum_{m=0}^{\infty}\frac{(\mu'/T - \mu/T)^m}{m!}W_{n+m}(\mu/T), \tag{B3}$$

where we have used a relation

$$\frac{\partial^m W_n}{\partial(\mu/T)^m} = W_{n+m}. \tag{B4}$$

We truncate the expansion up to $m = 3$ and their explicit forms for $n = 1, 2, 3, 4$ are given by

$$W_1(\mu'/T) = W_1 + (\mu'/T - \mu/T)W_2 + \frac{(\mu'/T - \mu/T)^2}{2}W_3 + \frac{(\mu'/T - \mu/T)^3}{3!}W_4, \tag{B5}$$

$$W_2(\mu'/T) = W_2 + (\mu'/T - \mu/T)W_3 + \frac{(\mu'/T - \mu/T)^2}{2}W_4 + \frac{(\mu'/T - \mu/T)^3}{3!}W_5, \tag{B6}$$

$$W_3(\mu'/T) = W_3 + (\mu'/T - \mu/T)W_4 + \frac{(\mu'/T - \mu/T)^2}{2}W_5 + \frac{(\mu'/T - \mu/T)^3}{3!}W_6, \tag{B7}$$

$$W_4(\mu'/T) = W_4 + (\mu'/T - \mu/T)W_5 + \frac{(\mu'/T - \mu/T)^2}{2}W_6 + \frac{(\mu'/T - \mu/T)^3}{3!}W_7. \tag{B8}$$

We approximate $W_5 = W_7 = \mathrm{tr}[B]$ and $W_6 = \mathrm{tr}[C]$. The error of this approximation is suppressed by $(\Delta\mu/T)^n/n!$, and is relatively unnoticeable compared to the statistical error.

In this way, we obtain the difference $\Delta W_n(\mu'/T, \mu/T)$, and then from this one can construct the difference of any quark number–related observable.

[1] Z. Fodor and S. Katz, Phys. Lett. B **534**, 87 (2002).
[2] M. D'Elia and M.-P. Lombardo, Phys. Rev. D **67**, 014505 (2003).
[3] S. Kratochvila and P. de Forcrand, Proc. Sci., LAT2006 (2006) 167.
[4] M. Fukugita and A. Ukawa, Phys. Rev. Lett. **57**, 503 (1986).
[5] R. Gupta, G. Guralnik, G. W. Kilcup, A. Patel, and S. R. Sharpe, Phys. Rev. Lett. **57**, 2621 (1986).
[6] E. Kovacs, D. Sinclair, and J. Kogut, Phys. Rev. Lett. **58**, 751 (1987).
[7] J. Kogut, H. Wyld, F. Karsch, and D. Sinclair, Phys. Lett. B **188**, 353 (1987).
[8] S. A. Gottlieb, W. Liu, D. Toussaint, R. Renken, and R. Sugar, Phys. Rev. D **35**, 3972 (1987).
[9] M. Fukugita, H. Mino, M. Okawa, and A. Ukawa, Phys. Rev. Lett. **65**, 816 (1990).
[10] Y. Iwasaki, K. Kanaya, S. Sakai, and T. Yoshie, Z. Phys. C **71**, 337 (1996).
[11] S. Takeda, Y. Kuramashi, and A. Ukawa, Phys. Rev. D **85**, 096008 (2012).
[12] J. Danzer and C. Gattringer, Phys. Rev. D **78**, 114506 (2008).
[13] K. Nagata and A. Nakamura, Phys. Rev. D **82**, 094027 (2010).
[14] A. Alexandru and U. Wenger, Phys. Rev. D **83**, 034502 (2011).
[15] A. Li, A. Alexandru, K.-F. Liu, and X. Meng, Phys. Rev. D **82**, 054502 (2010).
[16] S. Takeda, X.-Y. Jin, Y. Kuramashi, Y. Nakamura, and A. Ukawa, Proc. Sci., LATTICE2012 (2012) 066.
[17] Y. Iwasaki, University of Tsukuba Report No. UTHEP-118, 1983 (unpublished).
[18] A. M. Ferrenberg and R. H. Swendsen, Phys. Rev. Lett. **63**, 1195 (1989).
[19] X.-f. Meng, A. Li, A. Alexandru, and K.-F. Liu, Proc. Sci., LATTICE2008 (2008) 032.
[20] C. Allton, M. Doring, S. Ejiri, S. Hands, O. Kaczmarek, F. Karsch, E. Laermann, and K. Redlich, Phys. Rev. D **71**, 054508 (2005).
[21] S. Aoki *et al.* (CP-PACS Collaboration, JLQCD Collaboration), Phys. Rev. D **73**, 034501 (2006).
[22] Y. Nakamura and H. Stuben, Proc. Sci., LATTICE2010 (2010) 040.
[23] J. Sexton and D. Weingarten, Nucl. Phys. **B380**, 665 (1992).
[24] T. Takaishi and P. de Forcrand, Phys. Rev. E **73**, 036706 (2006).
[25] M. Fukugita, M. Okawa, and A. Ukawa, Nucl. Phys. **B337**, 181 (1990).
[26] M. S. Challa, D. Landau, and K. Binder, Phys. Rev. B **34**, 1841 (1986).
[27] P. de Forcrand and V. Laliena, Phys. Rev. D **61**, 034502 (2000).
[28] Y. Sasai, A. Nakamura, and T. Takaishi, Nucl. Phys. B, Proc. Suppl. **129–130**, 539 (2004).
[29] M. Hanada, Y. Matsuo, and N. Yamamoto, Phys. Rev. D **86**, 074510 (2012).
[30] X.-Y. Jin, Y. Kuramashi, Y. Nakamura, S. Takeda, and A. Ukawa (unpublished).